WDR31 is a novel ciliopathy protein displaying functional redundancy with GTPase-activating proteins ELMOD and RP2 in recruiting BBSome to cilium

Sebiha Cevik[1*], Lama Alabdi[2,5*], Xiaoyu Peng[3], Tina Beyer[4], Atiyye Zorluer[1], Mustafa S. Pir[1], Ferhan Yenisert[1], Ranad Shaheen[2], Franziska Woerz[4], Felix Hoffmann[4], Betul Altunkaynak[1], Betul Pir[1], Karsten Boldt[4], Asli Karaman[7], Miray Cakiroglu[7], S. Sadik Oner[6,7], Ying Cao[3], Marius Ueffing[4], Fowzan S. Alkuraya[2], Oktay I. Kaplan[1]†

1- Rare Disease Laboratory, School of Life and Natural Sciences, Abdullah Gul University, Kayseri, Turkey

2- Department of Translational Genomics, Center for Genomic Medicine, King Faisal Specialist Hospital and Research Center, Riyadh, Saudi Arabia.

3- School of Life Sciences and Technology, Tongji University, Shanghai 200092, China

4- Institute for Ophthalmic Research, Centre for Ophthalmology, University of Tuebingen, Elfriede-Aulhorn-Strasse 7, D-72076 Tuebingen, Germany.

5- Department of Zoology, College of Science, King Saud University, Riyadh, Saudi Arabia

6- Goztepe Prof. Dr. Suleyman Yalcin City Hospital, Istanbul, Turkey

7- Science and Advanced Technology Application and Research Center, Istanbul Medeniyet University, Istanbul

*These two authors contributed equally to this work

† Correspondence to oktay.kaplan@agu.edu.tr

Abstract

The term "ciliopathy" refers to a group of over 35 rare disorders characterized by defective cilia and many overlapping clinical features, such as hydrocephalus, cerebellar vermis hypoplasia, polydactyly, and retinopathy. Even though many genes have been implicated in ciliopathies, the genetic pathogenesis in certain cases remains still undisclosed. Here, we identified a homozygous truncating variant in *WDR31* in a patient with a typical ciliopathy phenotype encompassing congenital hydrocephalus, polydactyly, and renal agenesis. WDR31 is an evolutionarily conserved protein that localizes to the cilium and cilia-related compartment. Analysis from zebrafish supports the role of *WDR31* in regulating the cilia morphology. The CRISPR/Cas9 knock-in (p.Arg261del) *C. elegans* model of the patient variant (p.Arg268*) reproduced several cilia-related defects observed in *wdr-31* null mutants. Mechanistic analysis from *C. elegans* revealed that WDR-31 functions redundantly with ELDM-1 (ELMOD protein) and RPI-2 (RP2) to regulate the IFT trafficking through controlling the cilia entry of the BBSome. This work revealed WDR31 as a new ciliopathy protein that regulates IFT and BBSome trafficking.

Introduction

Cilia are structurally and functionally distinct cellular projections, consisting of a microtubule-based axoneme extending from a centriole-derived basal body anchored at the plasma membrane. Cilia consist of multiple sub-compartments (basal body, transition zone, and ciliary tip) that display different protein compositions and structure (Blacque and Sanders, 2014; Rosenbaum and Witman, 2002; Satir and Christensen, 2007). Motile cilia mediate the movement of unicellular organisms such as *Chlamydomonas reinhardtii* or are involved in fluid movement across a tissue surface (Silflow and Lefebvre, 2001; Sleigh, 1989). Non-motile cilia, also known as primary cilia, possess mechanosensory, chemosensory, and osmosensory functions, and coordinate a range of extrinsic signaling pathways involved in cellular behavior, tissue development, and homeostasis such as those mediated by Hedgehog (Hh), Wnt, and receptor tyrosine kinase ligands (e.g. PDGFα) (Anvarian et al., 2019; Bloodgood, 2009; Nachury, 2014; Scholey, 2007).

The relation between cilia and human disorders has led to a greater understanding of their importance for human health. Both motile and primary cilia have been linked to the heterogeneous class of diseases known as ciliopathies, including Joubert Syndrome, Meckel Syndrome (MKS), and Nephronophthisis (NPHP). Owing to the presence of cilia on most cell types, ciliary defects result in varying multiorgan phenotypes such as kidney defects, retinitis pigmentosa, pancreatic cysts, hearing loss, congenital heart disease, and polydactyly (Reiter and Leroux, 2017; Wheway et al., 2019).

Over the last twenty years, there has been a large effort to reveal the molecular composition of cilia and its sub-compartments using several independent approaches, including clinical genomics, proteomics, functional genomics, and bioinformatics (Arnaiz et al., 2009; Avidor-Reiss et al.,

2004; Blacque et al., 2005; Breslow et al., 2018; Choksi et al., 2014; Jensen et al., 2016, p. 26595381; Lambacher et al., 2016; Li et al., 2004; Mick et al., 2015; Piasecki et al., 2010; Ruiz García et al., 2019; Shaheen et al., 2016; Shamseldin et al., 2020; Sigg et al., 2017; UK10K Rare Diseases Group et al., 2016; van Dam et al., 2019). Many proteins that make up the cilium, as well as many proteins that regulate cilia biology, have been identified. These collective efforts have resulted in the identification of 302 genes that are certain to be involved in cilia biogenesis, as well as over 180 ciliopathy genes. CiliaCarta estimates the total number of the ciliary genes to be about 1200 genes, implying that many more ciliary proteins and ciliopathy genes are yet to be discovered. Indeed, the genetic diagnosis of many ciliopathy disorders is still unknown (Shamseldin et al., 2020, 2020; SYSCILIA Study Group et al., 2013; van Dam et al., 2019; Wheway et al., 2019).

Owing to the lack of protein-synthesizing machinery in cilia, structural components of cilia and cilia cargos must be transported to cilia in order to construct and sustain cilia, and mutations in genes involved in ciliary trafficking are commonly seen in ciliopathies. Cilia has a one-of-a-kind protein delivery system called intraflagellar transport (IFT). IFT is made up of multisubunit protein complexes that travel bidirectionally along the cilia. The IFT complex contains two sub-complexes, IFT-A and IFT-B, consisting of 6 and 16 protein subunits, respectively (Prevo et al., 2017). The IFT-B sub-complex and Kinesin-2 motors mediate the motility of IFT and IFT cargos from the base of the cilia to the tip of the cilia (anterograde IFT), while the IFT-A sub-complex and the cytoplasmic dynein-2 motor facilitate the retrograde IFT transport (from the cilia tip to the base of the cilia) (Blacque, 2008; Rosenbaum and Witman, 2002). The IFT-A is involved in the transport of certain membrane proteins into cilia (Lee et al., 2008; Liem et al., 2012; Mukhopadhyay et al., 2010). Mutations in genes encoding IFT components lead to defects in cilia

91 formation in all examined organisms, indicating the importance of IFT for cilia assembly (Pazour
92 et al., 2000; Prevo et al., 2017).

93 Bardet–Biedl syndrome (BBS) was classified as a ciliopathy in 2003, and eight of the highly
94 conserved Bardet-Biedl syndrome proteins (BBS1, BBS2, BBS4, BBS5, BBS7, BBS8, BBS9, and
95 BBIP10) establish a stable protein complex called the BBSome that undergoes IFT. Work from a
96 range of organisms implicates the BBSome in a variety of cilia related process including acting as
97 a cargo adaptor for removing proteins from cilia and as a regulator of the assembly and stability
98 of IFT trains (Ansley et al., 2003; Lechtreck et al., 2009; Loktev et al., 2008; Nachury et al., 2007;
99 Nozaki et al., 2019; Ou et al., 2007, 2005; Wei et al., 2012; Williams et al., 2014; Xu et al., 2015;
100 Ye et al., 2018). For example, in the nematode *C. elegans* mutants lacking *bbs-7* or *bbs-8*,
101 detachment of IFT-A and IFT-B in the amphid cilia was reported in the anterograde direction (Ou
102 et al., 2005). Analysis with a hypomorphic mutant (*bbs-1*) revealed that BBSome is involved in
103 attaching IFT-B components to the retrograde IFT machinery at the ciliary tips in the channel cilia
104 of *C. elegans* (Wei et al., 2012).

105 To identify new ciliopathy genes, we focused on our single-cell RNA-seq data that compared
106 expression profiles of ciliated cells with those of non-ciliated cells in the nematode *C. elegans,* and
107 this work revealed novel cilia genes, including *WDR31* (manuscript in preparation). Our gene
108 discovery approach in combination with the use of clinical genetic testing and experimental
109 validations identified *WDR31* (WD repeat domain 31) as a novel ciliopathy gene encoding a highly
110 conserved cilia-associated protein. Our work from Zebrafish and *C. elegans* provides significant
111 insight into the function of WDR31 in cilia biogenesis. First, our work from *C. elegans* revealed
112 that WDR-31 functions redundantly with two GTPase activating proteins (GAPs) ELMD-1 (the
113 sole ortholog of the human ELMOD proteins) and RPI-2 (human retinitis pigmentosa 2

114 orthologue) to control the cilia morphology. Second, knocking out *wdr-31* along with *elmd-1* or
115 *elmd-1;rpi-2* causes IFT trafficking to be disrupted, resulting in ciliary tip accumulations of IFT-
116 B components and the OSM-3/KIF17 motor, as well as significantly reduced BBSome recruitment
117 to cilia. Taken together, WDR31 is a new ciliopathy-associated protein that exhibits functional
118 redundancy with two GAP proteins (ELMOD and RP2) in regulating cilia morphology and IFT
119 trafficking.
120

121 **Material and Methods**

122 ***C. elegans* strains, maintenance and genetic crossing**

123 For strain maintenance and genetic crosses, a standard procedure was followed, as described by
124 Sidney Brenner in 1974 (Brenner, 1974). After genetic cross with a marker to generate single,
125 double and triple mutants, we used the PCR strategy to trace the mutations in following mutants:
126 *wdr-31(T05A8.5)(tm10423)II.; wdr-31(tur003)II.; wdr-31(syb1568)II.; nphp-4(tm925)V.; mks-*
127 *6(gk674)I.; elmd-1(syb630) III.; RB1550 rpi-2(K08D12.2)(ok1863) IV.*; and *bbs-8(nx77) V*.
128 Primers can be found in Table S1.
129

130 **Lipophilic fluorescent dye-uptake assay and rescue analysis**

131 Healthy mixed-staged animals were collected using M9 buffer (3 g/L KH2PO4, 6 g/L Na2HPO4,
132 5 g/L NaCl, 1 mM MgSO4), centrifuged for 1 minute at 2000 rpm, and washed twice with M9
133 buffer to remove any bacterial contaminations. Worms were incubated for 45-60 minutes at room
134 temperature in an M9 buffer containing lipophilic dye (1:200 dilution in M9, Invitrogen™
135 Vybrant™ DiI Cell-Labeling Solution) (Herman and Hedgecock, 1990). The worms were then
136 washed twice with M9 before being moved to a new NGM plate. Wild type was always included

137 in Dye filling assay, and the dye uptake control for the wild type was performed under a stereotype
138 fluorescence microscope, followed by imaging with the fluorescence upright microscope. For the
139 rescue experiment, *N2;turEx24[arl-13p::GFP::elmd-1 (C56G7.3)::unc-54 3'UTR +rol-6}*
140 (OIK1045) were crossed into *wdr-31(T05A8.5)(tm10423)II., elmd-1(syb630) II,* double and *wdr-*
141 *31(T05A8.5)(tm10423)II., elmd-1(syb630) II, rpi-2(K08D12.2)(ok1863) IV.* triple mutants.
142 *N2;turEx21[arl-13p::wdr-31 (T05A8.5)::GFP::unc-54 3'UTR +rol-6} (1 ng)* (OIK1042) were
143 mated with *T05A8.5(syb1568)II., elmd-1(syb630) II, rpi-2(K08D12.2)(ok1863) IV.* triple mutants.
144 Plasmid (*arl-13p::wdr-31 (T05A8.5)::GFP::unc-54 3'UTR*) was directly microinjected into triple
145 mutant *T05A8.5(syb1568)II., elmd-1(syb630) II, rpi-2(K08D12.2)(ok1863) IV* (1 ng). *dpy-*
146 *5(e907);nxEx386[rpi-2::gfp + dpy-5(+)]* (MX352) were crossed into *wdr-*
147 *31(T05A8.5)(tm10423)II., elmd-1(syb630) II, rpi-2(K08D12.2)(ok1863) IV.* triple mutants. Three
148 independent Dye uptake assays were performed, and fluorescence filters were set for GFP and
149 Texas Red, followed by fluorescence imaging. Dye uptake of mutants with corresponding
150 transgenics strains was compared to that of non-transgenic strains in the same rescue plates **(Fig.**
151 **S2C, D)**.
152

153 **Generation of mutants using CRISPR/Cas9 in the nematode *Caenorhabditis elegans***

154 To generate *wdr-31(T05A8.5)(tur003)* allele, three sgRNAs targeting *C. elegans* T05A8.5 (human
155 WDR-31) were chosen using an online tool, Benchling [Biology Software] (2019), followed by
156 ordering complementary oligonucleotides (Macrogen, South Korea), and cloning of sgRNAs into
157 an empty sgRNA vector pRB1017. The successful sgRNA insert was confirmed with colony PCR,
158 followed by plasmid isolation. Three sgRNAs (each 50 ng/µl) were injected into the gonads of
159 wild type together with pDD162 (*Peft-3::Cas9;* 15 ng/ µl plasmid pRF4) and pRF4 (50 ng/ µl

160 plasmid pRF4) (Dickinson et al., 2013). F1s with the roller phenotype were identified, and after
161 they generated enough progenies, the PCR technique was used to identify the F1 generation
162 bearing the predicted deletion, as well as the homozygosity of the allele mutation. The PCR
163 products from knockout animals were then sent to the Sanger sequencing (Macrogen, South
164 Korea). *wdr-31(*tur003*)II.* mutants have 1276-bp deletion covering a huge part of exon II (297 bp
165 out of 359 bp) and whole exon III, IV, and exon V. This is likely a null allele of *wdr-31.* sgRNA
166 sequences can be found in Table S1.
167

168 **Generation of transgenic strains and strain list for *C. elegans***

169 To generate transgenic lines for localization, rescue experiments, and expression patterns, we
170 generated the following transgenic animals via microinjections.

171 *OIK1042 turEx21[arl-13p::wdr-31 (T05A8.5)::GFP::unc-54 3'UTR +rol-6}*;
172 *T05A8.5(syb1568)II., elmd-1(syb630) II, rpi-2(K08D12.2)(ok1863) IV.* (1 ng)

173 *OIK1044 N2;turEx23[elmd-1p::GFP::elmd-1 (C56G7.3)::unc-54 3'UTR +rol-6}* (5 ng)

174 *OIK1045 N2;turEx24[arl-13p::GFP::elmd-1 (C56G7.3)::unc-54 3'UTR +rol-6}* (5 ng)

175 *OIK1046 N2;turEx25[elmd-1p(C56G7.3)::GFP::unc-54 3'UTR +rol-6}* (50 ng)

176 *OIK1047 N2;turEx26[wdr-31 (T05A8.5)p::GFP::unc-54 3'UTR +rol-6}* (50 ng)

177 The rol-6 plasmid (50 ng/ µl plasmid pRF4) was co-injected as the co-transformation marker. In
178 brief, the plasmids were delivered by microinjections into the gonads of 1-day adult worms.
179 Worms were initially transferred onto a 2.5% agarose pad prior (Halocarbon oil, Sigma: 9002-83-
180 9), followed by microinjection. The microinjection was done using a Zeiss Axio Vert.A1 inverted
181 microscope with DIC optics coupled with a Narishige Micromanipulator MMO-4. We next
182 manually inspected the plates to find successful transgenics animals.

183 **Wild Type and mutant alleles:** N2; *FX30333; wdr-31*(*T05A8.5)(tm10423)II.; OIK393*
184 *T05A8.5(tur003)II.; PHX1568 T05A8.5(syb1568)II.; nphp-4(tm925)V.; mks-6(gk674)I.;*
185 *PHX630, elmd-1(syb630) III.; RB1550 rpi-2(K08D12.2)(ok1863) IV.*; *MX52, bbs-8(nx77) V.* We
186 obtained *wdr-31(T05A8.5)(tm10423)II. (FX30333)* mutant allele, which has a 160-bp deletion,
187 causing a frameshift, from the National Bioresource Project, Japan. The *wdr-*
188 *31(T05A8.5)(tm10423)II.* were outcrossed to wild type four times. The Caenorhabditis Genetics
189 Center (CGC), Minnesota, USA, provided the *RB1550 rpi-2(K08D12.2)(ok1863)* mutant, and the
190 *rpi-2(ok1863)* allele contains 1143-bp deletion that removes a large segment of exon III, exon IV,
191 and some portion of exon V. *T05A8.5(syb1568)II.* has 1888-bp deletion, deleting all exons except
192 exon I **(Fig. S3B)**. Sunybiotech created an independent null allele of *elmd-1* via CRISPR–Cas9.
193 The *PHX630, elmd-1(syb630) III.* mutant contains 1784-bp deletion, where except for exon I, all
194 exons were removed **(Supplementary Fig. 2B)**. *elmd-1(syb630) III.* were outcrossed to wild type
195 two times.
196
197 **Fluorescent transgenes for IFT proteins:** *GOU2162 che-3(cas443[gfp::che-3]) I; xbx-*
198 *1(cas502[xbx-1::tagRFP]) V ; GOU2362 ift-74(cas499[ift-74::gfp]) II.; EJP76 vuaSi15*
199 *[pBP36; Posm-6::osm-6::eGFP; cb-unc119(+)] I; unc-119(ed3) III; osm-6(p811) V;*
200 *N2;lqIs2[osm-6::gfp], N2;ejEx[osm-3::GFP + pRF4]; N2;ejEx[kap-1::gfp+pRF4]; EJP81*
201 *vuaSi24 [pBP43; Pift-140::ift-140::mCherry; cb-unc-119(+)]II; unc-119(ed3) III; ift-*
202 *140(tm3433) V; jhuEx [ift-140::GFP+pRF4]; Ex[rpi-2::GFP+ xbx-1::tdTomato+pRF4]; MX76*
203 *dpy-5(e907); nxEx(bbs-7::gfp+dpy-5 (+)).*
204 **Fluorescent transgenes for ciliary proteins:** PHX1180, *wdr-31(syb1180 [wdr-*
205 *31(T05A8.5)::GFP]); PHX1328, wdr-31(syb1328[wdr-31($^{R261\text{-}de)}$)::GFP])* (Disease mimicking

206 variant)*; OIK1042 N2;turEx21[arl-13p::wdr-31 (T05A8.5)::GFP::unc-54 3'UTR +rol-6} (5 ng);*
207 *OIK1044 N2;turEx23[elmd-1p::GFP::elmd-1 (C56G7.3)::unc-54 3'UTR +rol-6} (5 ng);*
208 *OIK1045 N2;turEx24[arl-13p::GFP::elmd-1 (C56G7.3)::unc-54 3'UTR +rol-6} (5 ng);*
209 *OIK1046 N2;turEx25[elmd-1p(C56G7.3)::GFP::unc-54 3'UTR +rol-6} (50 ng); OIK1047*
210 *N2;turEx26[wdr-31 (T05A8.5)p::GFP::unc-54 3'UTR +rol-6} (50 ng)*; *N2;Ex[mks-2::GFP +*
211 *tram-1::tdTOMATO + pRF4]; MX1409 N2; nxEx785[tax-4:gfp+ Posm-5::xbx-1::tdTomato +*
212 *rol-6(su1006)]; vuaSi21[pBP39; Pmks-6::mks-6::mCherry; cb-unc-119(+)]II; MX2418*
213 *N2;nxEx1259[pbbs-8::PLC-delta PH::GFP;MKSR-2::tdTomato; coel::GFP]; PY8847*
214 *oyIs65[str-1p::mcherry]; Ex[str-1p::nphp-4::gfp, unc122p::dsRed]*. All PHX strains were
215 generated using CRISPR/Cas9 by Sunybiotech. The list of extensive transgenic and mutant strains
216 was provided in Table S2.
217
218 **Fluorescence and Confocal microscopy for *C. elegans***
219 Fluorescence images (dye assay) and time-lapse movies (IFT movies) were captured using an epi-
220 fluorescence upright microscope (Leica DM6 B) (3 frames per second, and up to 120 frames). The
221 epi-fluorescence upright microscope was controlled with iQ3.6.2 Andor software and was attached
222 with an Andor iXon Ultra 897 EMCCD (an electron-multiplying charge-coupled device camera).
223
224 The LSM900 confocal microscope with Airyscan 2 (ZEN 3 Blue edition software) was used to
225 capture the high-resolution Z-stack images. On microscope slides, a drop of 2-3% agarose was
226 used to create an agarose pad, and worms were then moved to the agarose pad containing 1-3 µl
227 of 10 mM levamisole (an anesthetic agent). Images were collected at 0.14 m intervals with a Plan

228 ApoChromat 63x/1.40 NA target, then analyzed with Blue edition software ZEN 3 to create Z-
229 stacks, and processed with ImageJ (NIH) software (Schneider et al., 2012).
230
231 ***In vivo* intraflagellar transport assay for IFT frequency**
232 The time-lapse movies of GFP-labelled IFT proteins were analyzed with the automatic kymograph
233 analyzing tools KymographClear and KymographDirect, both of which are ImageJ based
234 (Mangeol et al., 2016). KymographClear was used to produce kymographs from time-lapse
235 movies. We examined each produced kymograph and calculated IFT frequency for IFT-74::GFP
236 (a single copy transgene), OSM-6::GFP (a single copy transgene), OSM-3::GFP, and IFT-
237 140::GFP in wild type, *wdr-31;elmd-1* double and *wdr-31;elmd-1;rpi-2* triple mutants.
238
239 **Osmotic Avoidance Assay for assessing cilia functions in *C. elegans***
240 Right before each experiment, we freshly prepared an 8M fructose solution containing
241 bromophenol blue and made a ring of 8M bromophenol blue solution using 1 ml pipette tips. 1-
242 day adult worms of wild type and *osm-5(p813)* mutants were always tested as positive and negative
243 controls before evaluating the mutant strains (Haycraft et al., 2001). Wild-type worms are
244 supposed to remain in the ring under normal conditions, while *osm-5(p813)* mutants may be able
245 to escape due to a defect in the cilia structure. Every assay lasted 5 minutes, and five worms were
246 placed in the ring. At least three separate experiments (on different days) were conducted for each
247 strain, and the total number of worms was more than 40 for wild type and *osm-5(p813),* and more
248 than 80 for the rest of mutants. Fig. S4A was a combined representation of the last two independent
249 experiments.
250

251 **Whole-mount *in situ* hybridization in zebrafish**

252 Whole-mount in situ hybridization was performed as previously described (Thisse et al., 2004).
253 The *wdr31* cDNA with T7 promoter was PCR amplified, with forward primer:
254 ATGGGGAAGCTACAGAGCAAGTTC and reverse primer:
255 TAATACGACTCACTATAGAAGCGAGCCACTTCAGTGATACTG, from a homemade
256 cDNA library of zebrafish embryos at 24 hpf. The antisense probe for *wdr31* was then transcribed
257 with digoxigenin-labeled UTPs and T7 RNA polymerases (Roche, Basel, Switzerland). The
258 stained embryos were dehydrated in glycerol and photographed with a Nikon SMZ1500
259 stereomicroscope (Nikon, Tokyo, Japan).

260

261 **Mutagenesis of *wdr31* in zebrafish using the CRISPR/Cas9 technology**

262 Generation of zebrafish mutants using the CRISPR/Cas9 system was carried out as previously
263 described (Chang et al., 2013). Briefly, two gRNAs targeting sequences in *wdr31* were chosen as
264 following: 5'- ACCCATGTGTGTTGGGTACC-3' and 5'-GAAGCCATCCAGGAGTTCAG-3'.
265 gRNA templates were PCR amplified and gRNAs were *in vitro* transcribed with T7 transcriptase
266 (NEB, cat# M0251S). gRNAs and Cas9 protein (NEB, cat# M0251S) were simultaneously injected
267 into the embryos at one-cell stage.

268

269 **Immunofluorescence staining and microscopy**

270 Immunostaining was performed as previously described (Xu et al., 2017). Briefly, embryos were
271 fixed in cold Dent's fixative (80% methanol: 20% dimethyl sulfoxide) at -20°C overnight and then
272 stored in methanol. Samples were permeabilized with 0.005% (m/v) trypsin for 30 minutes.
273 Samples were blocked with blocking buffer (10% [v/v] goat serum in PBST), followed by
274 incubation with primary antibody anti–acetylated tubulin (1:2000; Sigma-Aldrich, St. Louis, MO)

275 and then secondary antibodies conjugated with Alexa Fluor 568 (1:500; Invitrogen, Carlsbad, CA).
276 Samples were mounted on ProLong Gold Antifade Mountant with DAPI (Invitrogen) and images
277 were taken with a Nikon A1R confocal microscope.
278

279 **Software and algorithms**

280 Zen Blue	Zeiss	https://www.zeiss.com/corporate/int/home.html
281 Andor iQ3	Andor	https://andor.oxinst.com/
282 Fiji	ImageJ	https://fiji.sc
283 ImageJ	ImageJ	https://imagej.nih.gov/ij/
284 Illustrator (CS5.1)	Adobe, USA	https://www.adobe.com/
285 KymographClear	Peterman Lab	https://sites.google.com/site/kymographanalysis
286 R	R Core Team	https://www.r-project.org/

287

288 **Statistical analysis and Generating Figures**

289 For statistical analysis of dye assay, Fisher's exact test was performed. For data involving
290 continuous variables like IFT speed and cilia length, Mann-Whitney U-test or Welch's t-test was
291 used depending on the distribution of data. All statistical tests were performed using R software.
292 The codes and files needed to generate figures and perform statistical analysis were openly shared,
293 and the files and codes for making figures and performing statistical analysis may be accessed at
294 https://github.com/thekaplanlab/WDR31-ELMOD-RP2.

295 **Gateway Cloning (mammalian constructs)**

296 Constructs for ELMOD3 (HsCD00288286) and WDR31 (HsCD00045652) were purchased

297 from Harvard Medical School. LR Reaction (Invitrogen, USA) was performed to transfer the target
298 sequence into destination vectors ((N)RFP, (N)CFP plasmids) with a subsequent transformation
299 into E.coli DH5α. DNA was isolated according to Monarch® Plasmid Miniprep Kit (BioLabs,
300 USA) and the PureYield® Plasmid Midiprep Protocol System (Promega, USA). Verification of
301 successful cloning was done by sequencing (Eurofins, Luxembourg).
302
303 **Immunofluorescence Staining (Mammals)**
304 hTERT-RPE1 cells were transiently transfected according to Lipofectamine™ 3000 Reagent
305 Protocol with ELMOD3-CFP and WDR31-RFP constructs followed by serum starvation for three
306 days to induce cilia formation. Cells were fixed with 4% PFA for 45min at 4°C, permeabilized for
307 5min with 0.3% PBST and blocked with 10% goat serum in PBST at 4°C overnight. A primary
308 antibody for ARL13B (1:50; Proteintech, Germany) and a secondary antibody conjugated to Alexa
309 Fluor 647 (1:350; Invitrogen, USA) were used. Cells were mounted using Fluoromount-G
310 (Invitrogen, USA).
311 **Microscopy Setup (Mammals)**
312 Images were captured using a Leica TCS SP8 scanning microscope (Leica Microsystems IR
313 GmbH, Germany). The setup includes 488 nm, 532 nm and 635 nm pulsed excitation lasers as
314 well as 100x oil immersion objective lens (NA 1.4) and a hybrid detector (HyD). Pixel number
315 was 1024 x 1024 and optimal pixel size was determined by Nyquist calculation resulting in a size
316 of 43 × 43 nm in XY. Additionally, Z-steps should not exceed 131 nm when acquiring a stack.
317 Laser intensity was adjusted for each sample and images were recorded with 2x frame averaging.
318
319

320 **Image Processing (Mammals)**

321 Acquired images were processed (LasX, Leica Microsystems), deconvoluted (Huygens Software,
322 SVI, Netherlands) and edited (FIJI software). The deconvolution was performed with a Classical
323 Maximum Likelihood Estimation (CMLE) algorithm under experimentally defined settings. The
324 background level was software estimated, the quality threshold was 0.001, the number of iterations
325 was 50 and signal-to-noise ratio was set to 20. All images were brightness-corrected for the
326 purpose of presentation.

327

328 **Exome sequencing analysis.**

329 Informed written consent was obtained from all participants under an IRB approved protocol
330 (KFSHRC RAC# 2080006). Whole exome sequencing was performed on the DNA sample
331 collected from proband as previously described (Saudi Mendeliome Group, 2015). Variant
332 classification followed the recommendations of the American College of Medical Genetics
333 (Richards et al., 2015).

334 **Sequence analysis**

335 Sanger sequencing and segregation analysis were done for the proband and family members.

336 **Results**

337 **WDR31 and ELMOD are evolutionarily conserved constituents of cilia**

338 As part of our ongoing effort to reveal novel cilia genes, using single-cell RNA-seq data, we
339 conducted comparative expression analysis in *C. elegans* and discovered that the WDR31 and
340 ELMOD orthologues, WDR-31 (T05A8.5) and ELMD-1 (C56G7.3), are likely expressed
341 exclusively in ciliated sensory neurons (manuscript in preparation). The head (amphid) and tails

342 (phasmid) of *C. elegans* contain a total of 60 ciliated sensory neurons, and the expression patterns
343 of genes can be reliably analyzed using fluorescence tagged promoter markers. Consistent with
344 our predictions, promoter-based GFP reporters revealed that both WDR-31 and ELMD-1 are
345 expressed in most of the ciliated sensory neurons **(Fig. S1A)**. To explore if both proteins are
346 concentrated within cilia, we investigated their subcellular localization in *C. elegans* and created
347 CRISPR/Cas9-mediated knock-in of WDR-31::GFP and a transgenic animal expressing GFP-
348 tagged ELMD-1. The endogenously expressed WDR-31::GFP is concentrated at the ciliary base
349 in both head and tails, where it colocalizes with the basal body marker γ-tubulin (TBG-1, the
350 ortholog of human TUBG1), and the IFT-140 (human IFT140) basal body signal **(Fig. 1A, B, C,**
351 **and D)**, so our co-localization data suggests that WDR-31 is a new cilia-associated protein.
352 ELMD-1 is the sole orthologue of the three human ELMOD proteins (ELMOD1-3) that function
353 as GTPase-activating proteins (GAP). We found that GFP::ELMD-1 localizes to the periciliary
354 membrane compartment (PCMC) and the basal body (BB) (marked with IFT-140), but is proximal
355 to the MKS-6-labeled transition zone that is adjacent to the BB **(Fig. 1E, F, and G)** (Kaplan et al.,
356 2012).
357
358 To determine if both human WDR31 and ELMOD3 (also known RBED1, the top blastp hit for
359 *elmd-1*) are concentrated within cilia in mammalian cell lines, we generated hTERT-RPE1 cells
360 co-expressing WDR31-RFP and ELMOD3-CFP and stained them with a ciliary marker ARL13B.
361 Furthermore, WDR31-RFP or ELMOD3-CFP were transiently transfected into hTERT-RPE1
362 cells, and they were additionally stained for ARL13B. Our super-resolution microscopy analysis
363 revealed that both WDR31 and ELMOD3 are enriched in the cilium **(Fig. 2A, B and Fig. S2B**
364 **and C)**. Taken together, our complementary approach demonstrates that both WDR31 and
365 ELMOD3 are evolutionarily conserved proteins associated with cilia.

366 **A homozygous truncating WDR31 variant leads to a ciliopathy**

367 WDR31 is a poorly characterized gene encoding a 367 amino acid long conserved protein with
368 four WD domains, but with our WDR31 and ELMOD3 localization data, WDR31 and ELMOD3
369 emerge as a strong gene candidate for ciliopathy **(Fig. 3A)**. Our ciliopathy patient database was
370 scanned for the presence of mutations in *WDR31* and *ELMOD3,* and we identified a homozygous
371 nonsense variant (NM_001012361.2: c.802C>T; p.Arg268*, rs ID: rs764141336) in a ciliopathy
372 male patient. The conversion of the arginine residue at position 268 to a stop codon (R268*) in
373 WDR31 prevents the translation of the last 99 amino acids with a WD domain **(Fig. 3A)**. This
374 variant is very rare in gnomAD (MAF 0.0000239) and in our database of 2,379 ethnically matched
375 exomes (MAF 0.001). The patient possesses renal agenesis, congenital hydrocephalus, right
376 microtia, right preaxial polydactyly, and congenital heart disease **(Fig. 3B, C D, and E)**. Sanger
377 sequencing confirmed the existence of a homozygous nonsense variant in the affected male while
378 parents and two unaffected sisters (II:3, II:5) are heterozygotes for the mutation and unaffected
379 brother and sister (II:4) had the wildtype genotype **(Fig. 3F, G)**. Taken together, our clinical data
380 linked a novel cilia gene *WDR31* to a typical ciliopathy.

381

382 **Wdr31 regulates ciliogenesis in the Zebrafish ear**

383 We turned our interest into zebrafish to develop an in *vivo* model for WDR31 to examine the role
384 of WDR31. We first used the whole-mount *in situ* hybridization (ISH) within zebrafish to visualize
385 the expression pattern of *wdr31* during zebrafish embryo development up to 1-day post-
386 fertilization. The dynamic and wide expression of *wdr31* during zebrafish embryonic development
387 (2 cell and 8 somite stages (SS)) has become restricted to the otic vesicle and brain region at 24
388 hours post-fertilization (24 hpf) **(Fig. 4A)**. We next knocked out (KO) *wdr31* in zebrafish with the
389 CRISPR/Cas9 system and the embryos showed heart edema and otolith malformation. As *wdr31*

390 is expressed in the otic vesicle and the otolith development requires cilia, we checked the cilia in
391 the otic vesicle. The cilia bundle in the lateral crista (LC) of the otic vesicle was stained with
392 acetylated tubulin in wild type and *wdr31* KO, and although we found that the length of LC cilia
393 was comparable with wild type, the width of the cilia bundle was reduced by 33% in LC of the
394 otic vesicle compared to that in the control embryos, suggesting the cilia number is decreased **(Fig.**
395 **4B, C, and D).** Our zebrafish work indicates that WDR31 plays a role in ciliogenesis in the
396 zebrafish ear.
397

398 **Functional redundancy of WDR31, ELMOD, and RP2 for determining cilia morphology**

399 We next wanted to gain mechanistic insight into the functions of *wdr-31* in cilia biogenesis. To
400 this end, we employed the nematode *C. elegans* and obtained/generated three *wdr-31* alleles:
401 tm10423 (160-bp frameshift causing deletion), syb1568 (1888-bp deletion removing all exons
402 except exon I), and tur003 (1276-bp deletion removing a large portion of exon II and exon III, IV,
403 and exon V) (**Fig. S3B)**. In *C. elegans,* the lipophilic fluorescent dye-uptake assay is employed to
404 indirectly evaluate the cilia structure, and our analysis revealed *wdr-31* mutants display wild type
405 level dye-uptake in both head (amphid) and tail (phasmid), suggesting cilia structures are likely
406 unaffected in these mutants **(Fig. 4E)**. To address whether loss of *wdr-31* leads to subtle defects
407 in cilia morphology, we expressed the fluorescence-based marker *str-1pro:mCherry* that labels the
408 AWB cilia in *wdr-31* mutants. The AWB dendritic tip extends the fork-like cilia in the wild type,
409 and our confocal microscopy analysis showed that the structure and length of AWB cilia are
410 comparable with that of wild type AWB cilia, suggesting, contrary to the importance of WDR31
411 for ciliogenesis in the zebrafish ear, the loss of *wdr-31* alone does not result in a severe defect in
412 cilia structure **(Fig. 4B, D, and F)**. The lack of an apparent cilia phenotype in *C. elegans* may be

413 attributed to a functional redundancy for WDR-31 in cilia biogenesis, and functional redundancy
414 is indeed a common phenomenon in ciliopathy-related genes. For example, while the absence of
415 individual ciliopathy genes encoding MKS/MKSR proteins or NPHP proteins (NPHP-1, NPHP-
416 4) does not result in serious cilia defect, the loss of *nphp-4* (the ortholog of human NPHP4) in
417 combination with *mks-6* (the ortholog of human CC2D2A) causes more severe cilia related defects
418 (transition zone membrane association defects) (Williams et al., 2011). We next explored genetic
419 interaction between *wdr-31* and *elmd-1*, since our results showed that both protein products are at
420 the ciliary base **(Fig. 1C, D, E, and F)**. We discovered that the *wdr-31(tm10423);elmd-1(syb603)*
421 double mutant (hereinafter referred to as "double mutant") has a partial Dyf defect in both head
422 and tail neurons, which was rescued by expression of a transgene containing the wild type *elmd-1*
423 sequence **(Fig. 4E and Fig. S3C,** $p < 0.0001$, Fisher's exact test**)**. Using the AWB cilia
424 fluorescence marker, we subsequently set out to visualize the ciliary structures in the double
425 mutant and single mutants. The AWB cilia in the double mutants have an extra projection in the
426 middle part of the cilia, and the cilia are of normal length (7% (N: 100) and 52 % (N: 134) of extra
427 projections in WT and double mutant, respectively) **(Fig. 4F and G, and Fig. S4B, C and D)**.
428 We explored genetic interaction between *wdr-31, elmd-1,* and *rpi-2* (the X-linked retinitis
429 pigmentosa protein RP2 and a GTPase-activating protein) since ELMD-1 and WDR-31
430 localizations are reminiscent of RPI-2 localisation in *C. elegans* (**Fig. S5B)** (Williams et al., 2011).
431 We, therefore, first generated an elmd-1*;rpi-2* double mutant, which revealed no Dyf phenotype.
432 However, when we created *wdr-31;elmd-1;rpi-2* triple mutants (hereinafter referred to as "triple
433 mutant"), we observed severe synthetic Dyf phenotype, which is significantly rescued by the
434 introduction of a wild-type copy of *wdr-31* or *elmd-1 or rpi-2* **(Fig. 4E, Fig. S3C, D,** $p < 0.0001$,
435 Fisher's exact test**)**.

436 We then sought to examine AWB cilia morphology in triple mutants and compared it with the
437 *wdr-31;elmd-1* and *rpi-2;elmd-1* double mutants. The Dyf defect of triple mutants was indeed
438 accompanied by significant changes in the AWB cilia that displayed the ectopic projections,
439 including a backward projection from the base of AWB cilia in all three independent *wdr-31* alleles
440 and as wells as ectopic projections from the middle part of AWB cilia (0% backward projection in
441 wild type vs over 30% backward projection in triple mutants; $p < 0.0001$, Fisher's exact test), but
442 the length of AWB cilia (long) in triple mutants was similar to that of wild type **(Fig. 4F, F, and**
443 **Fig. S4B, C, D)**.
444
445 Finally, we investigated the effect of *wdr-31, rpi-2* and *elmd-1* loss on osmotic avoidance
446 behaviour which is mediated by sensory cilia. Our analysis showed that double and triple mutants
447 display defective osmotic avoidance (Osm) behaviour, suggesting cilia are not functioning
448 properly (**Fig. S4A**).
449
450 **Loss of WDR-31 and ELMD-1 leads to the ciliary accumulations of OSM-3/KIF17 Kinesin**
451 **motor and Complex B components**
452 We next aimed to investigate the mechanism by which WDR-31, ELMD-1, and RPI-2 regulate
453 cilia morphology in *C. elegans.* To this end, we investigated whether these genes affect the
454 localization of IFT proteins and IFT motors, including kinesin motors (Kinesin II and OSM-
455 3/KIF17), dyneins, and IFT components (IFT-A and IFT-B). The IFT complex and motor proteins
456 are critical for cilia construction and maintenance because they deliver ciliary constituents from
457 the cell body to the cilia. In *C. elegans,* two kinesin motors Kinesin II and OSM-3/KIF17
458 (heterotrimeric kinesin-II and homodimeric OSM-3) work cooperatively to carry the IFT complex
459 in the middle segment of the channel cilia in an anterograde direction, while OSM-3/KIF17

460 transports the entire IFT complex (IFT-A, IFT-B, and BBSome) in the distal part of channel cilia.
461 We generated single, double, and triple mutants expressing fluorescence tagged IFT and motor
462 proteins. Using single-copy transgenes, we found that IFT-B components accumulate at cilia tips
463 and/or middle of cilia in double mutants (96% ciliary tip accumulations for IFT-74/IFT74, N: 26
464 and 82% ciliary tip accumulations for OSM-6/IFT52, N: 46) but the localization of GFP::CHE-3
465 (human dynein heavy chain DYNC2H1) remains less affected in double mutants (27% minor
466 middle cilia accumulations for CHE-3; N: 48, see supplementary Movie S1) **(Fig. 5A, C and D**
467 **and Supplementary Movie S1, 2, 4)**. Furthermore, we next investigated the localization of
468 GFP::CHE-3 in triple mutants because the cilia morphology of triple mutants is more severe than
469 that of *wdr-31;elmd-1* or *wdr-31;rpi-2* or *elmd-1;rpi-2* double mutants (**Fig. 5F).** Compared with
470 wild type and double mutants, we noticed additional IFT abnormalities in two independent triple
471 mutants, including dim cilia staining with GFP::CHE-3 and accumulations of GFP::CHE-3 in the
472 middle/distal part of cilia (81% middle cilia accumulations, N: 96; 6.6% ciliary tip accumulations,
473 N: 90) (**Fig. 5A and Supplementary Movie S1)**. Motor protein OSM-3/KIF17 accumulation
474 within the ciliary tips was detected in double and triple mutants. The size of OSM-3 ciliary tip
475 accumulations appeared to be larger in triple mutants than in double mutants **(Fig. 5B, and**
476 **Supplementary Movie S3)**. Furthermore, in triple mutants, the dim distal cilia staining was
477 observed for IFT-140::GFP (IFT-A component) (63% dim distal cilia, N: 47) and XBX-
478 1::mCherry (a dynein light intermediate chain) **(Fig. 5E and F and Supplementary Movie S5)**,
479 but the localization and motility of KAP-1::GFP (Kinesin II) remain unaffected **(Fig. 5G)**. Our
480 fluorescence microscopy analysis suggests defects in the return of IFT and OSM-3/KIF17 kinesin
481 motors from the cilia in double and triple mutants. We hypothesized that certain IFT particles
482 would be unable to return from the ciliary tips due to potential defects in the IFT returning, so we
483 measured IFT particle frequency in wild type and affected mutants to explore if the number of IFT

484 particles entering into cilia is affected and/or if the return of IFT particles from the ciliary tips is
485 altered. Using time-lapse video coupled with kymography, for a subset of IFT components, we
486 discovered a substantial reduction in the number of IFT particles traveling along the cilia in both
487 directions in double and triple mutants (**Fig. 6A, and B**). In wild type, the average of IFT-74
488 particles moving in anterograde and retrograde directions (33 seconds and 7.5 μm) is 19 and 17,
489 respectively, while in triple mutants, the anterograde and retrograde IFT-74 particles are 9 and 3.
490 Comparable reductions were observed for IFT-74::GFP (a single copy transgene) in *wdr-31;eldm-*
491 *1* (the anterograde and retrograde: 19 and 17 in wild type vs 12 and 7 in *wdr-31;eldm-1;* $p < 0.0001$;
492 the Mann–Whitney U test). However, for OSM-6::GFP, the retrograde IFT particles statistically
493 differ between wild type and triple mutants (the retrograde: 19 in wild type, 13 in double mutants*;*
494 and 11 in triple mutants*;* $p < 0.0001$; the Mann–Whitney U test) (**Fig. 6B**). Furthermore, we found
495 significant decline in the IFT transport for OSM-3::GFP in double and triple mutants in both
496 anterograde and retrograde directions, but the decrease in IFT transport was more severe for triple
497 mutants (the anterograde and retrograde: 23 and 20 in wild type; 16 and 11 in double mutants; 11
498 and 8 in triple mutants*,* $p < 0.0001$; the Mann–Whitney U test) (**Fig. 6B**). On the other hand, the
499 flux of cytoplasmic dynein motor protein CHE-3 along the cilium was unchanged in both
500 directions in both double and triple mutants, while FT-140 transport declined in both directions
501 **(Fig. 6B)**. Our findings suggest that with the exception of heterotrimeric Kinesin II, all IFT proteins
502 studied, including dynein CHE-3, OSM-3 kinesin, IFT-B, and IFT-A components, display certain
503 defects in *wdr-31* related mutants, either ciliary accumulations for dynein CHE-3, OSM-3 and
504 IFT-B component or dim distal cilia staining for IFT-A component and dynein motors (CHE-3
505 and XBX-1).
506
507

508 **The ciliopathy associated variant in WDR-31 displays cilia defects in *C. elegans***

509 Like human WDR31, *C. elegans* WDR-31 has WD-repeat domains **(Fig. 3A, and Fig. S2A).** In
510 the ciliopathy patient, we found the arginine-to-a termination codon substitution at residue 268 of
511 human WDR31 that removes the 99 amino acids containing a WD domain, but the functional
512 significance of this change is currently unknown in the context of cilia biogenesis. To investigate
513 whether the last 99 amino acids in WDR-31 is essential for the subcellular localization of WDR-
514 31 to the cilia base and the function of WDR-31, the CRISPR/Cas9 was used to engineer the *C.*
515 *elegans* model harboring the corresponding WDR31 deletion (named WDR-31$^{R261\text{-}del}$) **(Fig. 7A)**.
516 Using confocal microscopy, we determined the subcellular localization of WDR-31$^{R261\text{-}del}$, which
517 revealed that, similar to wild type WDR-31::GFP (Cas9/CRISPR GFP knock-in), WDR-31$^{R261\text{-}}$
518 ^{del}::GFP is situated at the base of cilia proximal to the MKS-6 marked transition zone (**Fig. 7B,**
519 **and Fig. S5A)**, suggesting that the last WD repeat within WDR-31 are not necessary for the ciliary
520 base localization. In contrast, we found several cilia abnormalities when the *wdr-31$^{R261\text{-}del}$* variant
521 was combined with *elmd-1* and *rpi-2.* First, similar to *wdr-31;elmd-1*;*rpi-2* triple mutants, the triple
522 *wdr-31$^{R261\text{-}del}$;elmd-1*;*rpi-2* mutants exhibit a synthetic Dyf phenotype, suggesting structural
523 defects in cilia in this triple mutant (**Fig. 4E, 7C**). Consistent with this expectation, we find that
524 the AWB cilia structural abnormalities in *wdr-31$^{R261\text{-}del}$;elmd-1*;*rpi-2*, including backward
525 projections from the cilia base, were comparable to three separate *wdr-31* mutants **(Fig. 4G, 7D,**
526 **E,** over 30% backward projection in triple mutants; $p < 0.0001$, Fisher's exact test**)**. As expected,
527 we observe no Dyf phenotype and cilia structural defects in *wdr-31$^{R261\text{-}del}$* single mutants (**Fig. 7C,**
528 **D)**.

529 Finally, because WDR-31, ELMD-1, and RPI-2 localize at the base of cilia, we wanted to examine
530 the role of these proteins in the ciliary gate, and we chose the TRAM-1 protein (the ortholog of
531 human TRAM1), which surrounds the PCMC in *C. elegans* but stays outside of cilia (Williams et

532 al., 2011). Our confocal microscopy analysis revealed that the TRAM-1 protein enters into cilia in
533 all examined *wdr-31* triple mutants, including *wdr-31*$^{R261\text{-}del}$*;elmd-1*;*rpi-2* but not in *wdr-31*$^{R261\text{-}del}$
534 single mutants (**Fig. 7E)**. Taken together, all these data from *C. elegans* indicates the human R268*
535 mutation (an equivalent of R261-del in *C. elegans*) in *WDR31* observed in the ciliopathy patient
536 is likely a pathogenic variant.
537
538 **WDR-31 and ELMD-1 are required for recruitment of BBS-7, a BBSome component, to cilia**
539 To find out the underlying reason for why IFT-B components and OSM-3/KIF17 specifically
540 accumulate at the ciliary tip in double and triple mutants, we hypothesized that the IFT complex
541 destabilization might be due to defects in the BBSome assembly. The IFT-B components were
542 previously reported to accumulate at the ciliary tip in BBSome mutants (Blacque, 2004; Wei et al.,
543 2012; Xu et al., 2015). We found that ciliary tip accumulations of IFT-74:GFP, an IFT-B
544 component, in *bbs-8(nx77)* mutants were comparably similar to that of double and triple mutants
545 (**Fig. 8A**). We next explored the localization of BBS-7::GFP, a core member of the BBSome, in
546 double and triple mutants. BBS-7::GFP is lost or significantly diminished in the cilia of double
547 and triple mutants, but BBS-7::GFP localization persists at the ciliary base in these mutants (**Fig.**
548 **8B**). The time-lapse movie analysis of BBS-7::GFP together with kymography reveals that BBS-
549 7::GFP movements were undetectable in 27% and 42% of cilia in the head in double and triple
550 mutants, respectively (**Supplementary Movie S6)**. We were able to quantify the frequency of
551 BBS-7::GFP even though the density of trajectories (IFT particles) on kymographs was weak in
552 double and triple mutants relative to wild type (**Fig. 8C**). Our analysis revealed a substantial
553 decrease in the average of BBS-7::GFP particles translocating in the anterograde and retrograde
554 directions in the remaining worms that display IFT (average anterograde and retrograde IFT

555 particles: 18 and 19 for wild type; 10 and 11 for double mutant; 2 and 2 for triple mutant, $p <$
556 0.0001; the Mann–Whitney U test) (**Fig. 8C, D and Supplementary Movie S6**). We next explored
557 the localization of transition fiber protein FBF-1 and TAX-4 (a membrane protein) in the triple
558 mutants because FBF-1 was implicated in the ciliary entry of IFT machinery (Wei et al., 2013).
559 Our data reveals that the localization of these proteins remains unaffected in the triple mutants
560 (**Fig. 5SB and D**). Taken together, our results suggest that because the BBSome complex is unable
561 to gain access to cilia in double and triple mutants, IFT-B components and OSM-3/KIF17 likely
562 accumulate excessively in the distal portion of the cilia while IFT Complex A component staining
563 the distal segment cilia become dim (**Fig. 8E**).
564

565 **Discussion**

566 **WDR31 is a new ciliopathy gene required for cilia biogenesis**

567 The list of both the primary and motile ciliopathy genes has been increasingly expanding with the
568 large-scale adoption of next-generation sequencing technologies in the exploration of genetic
569 causes for these diseases. So far, over 190 ciliopathy genes have been discovered (Wheway et al.,
570 2019). Despite substantial advances in identifying many ciliopathy genes, elucidating the
571 underlying genetic mutations and their functions in ciliopathies represent a major challenge. In the
572 current work, we identified *WDR31* as a novel cilia protein and relate it to ciliopathy. We found a
573 truncating variant in *WDR31* in a family of nine, with the only affected child harboring a
574 homozygous truncating variant. The patient displayed ciliopathy-related clinical features,
575 including congenital hydrocephalus, polydactyly, and congenital heart disease. The human
576 counterpart variant results in an abnormal cilia structure in *C. elegans*, confirming the conclusion
577 that this variant likely disrupts WDR-31 functions.
578

579 Human WDR31 is a member of the WD40-repeat protein (WDR) family, and it was previously
580 understudied even though several members of the WD40-repeat protein family, including WDR34,
581 WDR35, and WDR60, have been linked to cilia (Blacque et al., 2006; Patel-King et al., 2013;
582 Rompolas et al., 2007). Strikingly, we found that WDR31 is a ciliary protein, and knocking it out
583 in zebrafish using CRISPR/Cas9 causes ciliary defects, including a decrease in the number of cilia
584 in the LC. Furthermore, the link between WDR31 and cilia was significantly strengthened by
585 findings from *C. elegans*. First, the expression of the *WDR31* orthologue (WDR-31) is restricted
586 to the ciliated sensory neurons, and WDR-31 localizes to the base of cilia. The exclusive cilia
587 expression pattern of *wdr-31* in *C. elegans* is similar to that of ciliary and ciliopathy genes like
588 ARL-13/ALR13b, IFT, and BBS (Blacque et al., 2005). Second, CRISPR/Cas9 mediated knock
589 out of *WDR-31* combination with the ELMOD orthologue (ELMD-1) and RP2 orthologue (retinitis
590 pigmentosa 2; RPI-2) results in an abnormality in cilia functions and structure in *C. elegans*. Our
591 findings reveal that WDR31 is a new ciliopathy protein required for cilia morphology in both
592 zebrafish and *C. elegans*, suggesting the evolutionarily conserved role of WDR31 in cilia biology.
593

594 **Functional redundancy between WDR-31, ELMD-1, and RPI-2**

595 Our genetic analysis in *C. elegans* provides evidence for partial functional redundancy for *wdr-31*,
596 *elmd-1*, and *rpi-2* in regulating cilia morphology and the trafficking of kinesin-IFT-BBSome
597 complexes. Though cilia morphology is disrupted in *wdr-31;elmd-1;rpi-2* triple mutants, with
598 altered recruitment of kinesin, IFT, and BBS proteins, simultaneous elimination of *elmd-1* and *rpi-*
599 *2* did not result in severe defects in cilia and IFT. Our interpretation for these data is that the
600 additive defects in the triple mutants were likely due to *wdr-31*, and WDR-31 is a central player
601 in controlling cilia morphology and IFT machinery. However, we cannot rule out the possibility
602 of microtubule defects in cilia ultrastructure in *elmd-1;rpi-2* double mutants. Additional work is

603 needed, and a transmission electron microscope (TEM) may be used to reveal further details in the
604 ultrastructures of cilia in these double mutants.
605
606 How do these proteins work together to regulate cilia-related phenotypes? While WDR31 is a
607 poorly characterized gene, the roles of human RP2 and ELMOD proteins in cilia biology are better
608 understood. Human RP2 localizes to the cilium and the basal body and displays GAP activity
609 toward two ARF family members, ARL2 and ARL3, both of which were linked to cilia biology
610 (Evans et al., 2010; Schwarz et al., 2017; Wright et al., 2011), while the ELMOD protein family
611 (ELMOD1-3) has GAP activity for ARL2 (ELMOD1 and ELMOD3) and ARF6 (ELMOD1)
612 (Ivanova et al., 2014; Jaworek et al., 2013; Johnson et al., 2012; Miryounesi et al., 2019).
613 ELMOD2 localizes to the basal body, and our study showed ELMOD3 localizes to cilium (Turn
614 et al., 2021). Taking into account the fact that RPI-2 and ELMD-1 are GAPs, and loss of these two
615 GAP proteins likely result in the overactivation of their target G proteins, how does WDR-31
616 function with these GAP proteins? One possibility is that WDR31 may function downstream of
617 regulatory GTPases, including ARL2, ARL3, or unidentified GTPases, activated by these GAP
618 proteins. One downside of this explanation is that *wdr-31* single mutants did not have significant
619 ciliary and IFT defects; but, if this were valid, we would expect to observe further anomalies in
620 cilia and IFT in *wdr-31* single mutants, close to the removal of these three genes. Alternatively,
621 the activity/function of overactive GTPases can be somehow regulated by WDR-31, maybe WDR-
622 31 may have a GAP activity for the regulatory GTPases or it may have a GTPase activity. While
623 WDR-31 does not seem to have a GAP domain, HHMER search revealed that human WDR31 has
624 a distant sequence resemblance to a nucleoside-triphosphatase (NTPase) domain (NACHT)
625 containing protein in *Penicillium camemberti* (Gabler et al., 2020). PSI-BLAST search confirmed
626 this result (unpublished data).

627

628 Furthermore, the ciliary roles of these two GAP proteins might be independent of their GAP
629 activities, and consistent with this idea, the recent study showed the ciliary roles of ELMOD2 are
630 partially independent of its GAP activity (Turn et al., 2021). However, a variety of evidence
631 suggests that WDR31 and ELMOD3 do not form a complex. First, mass spectrometry-based
632 proteomic analysis for either WDR31 or ELMOD3 showed that neither WDR31 nor ELMOD3
633 contains each other or RP2 (unpublished data). Second, the proper localization of any of these
634 three proteins was independent of each other (unpublished data). Further studies are needed to
635 understand a mechanistic link between WDR31, ELMOD, and RP2, and figure out the independent
636 contributions of WDR31 and both GAP proteins in cilia biology.

637

638 **How does the WDR31-ELMOD-RP2 regulate the IFT trafficking in cilia?**

639 Based on our results, which involve a decrease in moving IFT particles in anterograde transport,
640 ciliary tip aggregation of OSM-3/KIF17 and IFT-B, and docking of BBSome to the IFT machinery,
641 we propose that these defects likely stem from the failure of BBSome to associate with moving
642 IFT in cilia in double and triple mutants. Consistent with our proposal, the almost comparable
643 IFT/BBSome phenotypes were reported with hypomorphic mutations in *dyf-2* (WDR19
644 orthologue, an IFT-A component) and *bbs-1* (a BBSome component), where they showed that
645 while BBSome remains at the base of cilia and does not undergo IFT, the failure of IFT-B
646 reassociation with IFT-A at the ciliary tips results in IFT-B ciliary tip accumulations, despite the
647 fact the association of IFT-A and IFT-B components in anterograde transport persists (Wei et al.,
648 2012). They proposed that the BBSome controls the IFT assembly at the ciliary base and IFT
649 turnover at the ciliary tip. However, the IFT defects in the triple mutant are unlikely to be due to
650 mislocalization of transition fiber proteins such as DYF-19 (the FBF1 orthologue), which was

651 implicated in regulating the ciliary entry of IFT and BBSome, since our data showed that the
652 localization of DYF-19 was not impaired in the triple mutants (Wei et al., 2013). On the other
653 hand, the effect on IFT might be direct since RP2 was previously proposed to control the
654 intraflagellar transport protein IFT20 pool in the peri-basal body and trafficking of Kif17 and Kif7
655 to the ciliary tip (Schwarz et al., 2017). However, several interesting questions have yet to be
656 resolved: what is the mechanism by which WDR-31-ELMD-1-RPI-2 regulates the ciliary entry of
657 the BBSome entry? How does WDR-31-ELMD-1-RPI-2 interact with proteins, including ARL6,
658 that regulate the BBSome recruitment (Jin et al., 2010)? Future study research will help us to
659 understand how these proteins regulate BBSome/IFT trafficking. In summary, this study provides
660 a mechanistic explanation of the function of WDR-31, a new ciliopathy protein, in the regulation
661 of cilia biogenesis and also contributes to our knowledge of the molecular etiology of WDR31
662 mediated disease.
663

664 **Acknowledgments**

665 We thank the family of the patient, who participated in the study. We thank Oliver Blacque, Piali
666 Sengupta, Micheal Leroux, the National BioResource Project (NBRP) in Japan, and the CGC in
667 the United States, which is financed by the NIH Office of Research Infrastructure Programs (P40
668 OD010440) for sharing valuable strains. We thank Oliver Blacque and Samuel Katz for critical
669 reading of the manuscript. We thank the Abdullah Gul University Scientific Research Project
670 Coordination Unit (Project number: TOA-2018-110) for providing the funding that initiated the
671 project. M.U. was supported by the Tistou & Charlotte Kerstan Stiftung. The Leica laser
672 scanning microscope was funded by a grant from Deutsche Forschungsgemeinschaft (INST
673 2388/62-1).
674

675 **Figure 1: WDR-31/WDR31 and ELMD-1/ELMOD proteins are evolutionary conserved**
676 **ciliary proteins A, B)** Shown are the representative drawing of the PHA/PHB sensory neuron
677 (phasmid neurons located in the tail). Cilia, dendrite, axon and cell soma (cell body) are depicted
678 in the drawing. Fluorescence images from the transgenic strain carrying WDR-31::GFP or
679 GFP::ELMD-1 were displayed in the PHA/PHB sensory neurons. Scale bars: 3 µm **C, D)** Co-
680 localization of WDR-31::GFP (Green) with the IFT-140::mCherry (Red, an IFT-A component, a
681 ciliary marker) or TBG-1:mKate (Red, γ-Tubulin, the basal body) in the tail (phasmids) and head
682 (amphid) sensory neurons. TZ and BB denote the transition zone and the basal body, respectively
683 **E, F)** GFP::ELMD-1 (Green) localizes to the BB and PCMC (the periciliary membrane
684 compartment) proximal to the transition zone. Co-labelling of GFP::ELMD-1 with MKS-
685 6:mCherry marker (transition zone) or IFT-140::mCherry in the tail (phasmids) and head (amphid)
686 neurons. Scale bars: 2 µm **G)**
687
688 **Figure 2**: **ELMOD3 and WDR31 localize to the primary cilium**. **A, B**) Shown are the staining
689 of WDR31 (tagged with cyan fluorescent protein) and ELMOD3 (tagged with red fluorescent
690 protein) together with a ciliary marker ARL13B and DAPI (nucleus) in hTERT-RPE1 cells.
691 hTERT-RPE1 cells were transiently transfected with 100 ng of WDR31:CFP and ELMOD3:RFP.
692 Scale bars: 10 µm (A) and 3 µm (B)
693
694 **Figure 3: A homozygous p.R268* variant in WDR31 leads to a ciliopathy A)** Shown is the
695 schematic of WDR31 (NP_660284.1), with 367 amino acids in length and WD domains as tandem
696 repeats. The position of disease associated p.R268* (rs ID: rs764141336) variant is depicted in
697 human WDR31, resulting in a 268 amino acid protein in length. **B and C)** Clinical images and

698 molecular analysis of the proband. Facial images of the proband (14DG0977) with hydrocephalus
699 and right microtia, **D and E)** X-ray imaging highlighting right preaxial polydactyly, and
700 hydrocephaly, respectively. **F)** schematic representation of the pedigree showing consanguinity
701 between the parents (1st degree cousins). The proband is marked with an arrow. **G)** Sequence
702 chromatogram confirming the variant segregation in the index (homozygote c.802C>T;
703 p.(Arg268*)). The parents and two unaffected sisters (II:3, II:5) are carriers (heterozygotes), and
704 the unaffected brother and sister (II:4) are wild types.
705
706 **Figure 4: WDR31 regulates ciliogenesis in zebrafish A)** Shown are the expression pattern
707 analysis of WDR31 in zebrafish embryos. *Wdr31* is ubiquitously expressed before the
708 segmentation stage (2 cell and 8 somite stages (SS). The expression of *Wdr31* becomes limited to
709 the otic vesicle and brain region at 24 hours post fertilization (24 hpf). Shown are cilia of lateral
710 crista (LC) of the otic vesicle, stained with acetylated-tubulin, in wild type and *Wdr31* knockout,
711 generated via CRISPR/Cas9. **C and D**) The length of cilia in the lateral crista (LC) of the otic
712 vesicle remains unaffected in zebrafish *Wdr31* knockout while the cilia number is decreased, as
713 shown with the measurement of width of cilia lateral crista (LC) of the otic vesicle. **E)** Shown are
714 the schematic representations of lipophilic fluorescent dye uptake in the head (amphid) and tail
715 (phasmid) sensory neurons in *C. elegans.* Red labelling indicates the normal dye uptake while the
716 failure of Dye uptake was shown in white. Fluorescence images show the dye update in the head
717 and tail neurons in the wild type and indicated mutant strains. No dye uptake was observed in both
718 head (amphid) and tail (phasmid) of *wdr-31(tm10423);elmd-1* double mutants, *wdr-*
719 *31(tm10423);elmd-1;rpi-2* and *wdr-31(syb1568);elmd-1;rpi-2* triple mutants. *Ex[elmd-1(+)*]
720 rescues the dye uptake defects of *wdr-31(tm10423);elmd-1* double and *wdr-31(tm10423);elmd-*

721 *1;rpi-2* triple mutants, while *Ex[wdr-31(+)]* rescues the Dye uptake defects of *wdr-*
722 *31(syb1568);elmd-1;rpi-2* triple mutants. Scale bars: 10 μm **F)** Fluorescence images show the
723 morphology of AWB cilia (fork-like structure located in the head) in wild type and indicated
724 mutant backgrounds. The backward projection from the cilia is shown with asterisks (*) while p
725 indicates the ectopic projections from the middle parts of cilia. The AWB cilia in wild type and
726 affected mutants are shown in schematic sketches.
727
728 **Figure 5: IFT-B proteins and OSM-3/KIF17 accumulate at the ciliary tip.** Shown are
729 fluorescent images of PHA/PHB cilia (phasmid tail). **A)** Fluorescent images from a single copy
730 GFP::CHE-3 (human dynein heavy chain DYNC2H1) in wild type and indicated mutant
731 backgrounds are displayed. GFP::CHE-3 accumulations within cilia and dim distal cilia staining
732 were observed in two distinct triple mutants (*wdr-31(tm10423);elmd-1;rpi-2* and *wdr-*
733 *31(syb1568);elmd-1;rpi-2).* Scale bars: 3 μm **B, C, D, E, F)** Confocal microscopy analysis of
734 IFT-A (IFT-140::GFP) and IFT-B complex components (OSM-6/IFT52::GFP and IFT-74::GFP)
735 revealed differential abnormalities in the transport of IFT-A and IFT-B components in double
736 (w*dr-31;elmd-1*) and triple mutants. The localization of XBX-1::mCherry (Dynein subunit) in
737 *wdr-31(syb1568);elmd-1;rpi-2* triple mutants phenocopies the dim distal cilia staining of IFT-A
738 (IFT-140::GFP) in the w*dr-31(tm10423);elmd-1;rpi-2* triple mutants. OSM-3/KIF17 Kinesin
739 motor accumulates at the ciliary tips in w*dr-31(tm10423);elmd-1* double and w*dr-*
740 *31(tm10423);elmd-1;rpi-2* triple mutants. Compared to double mutants, the ciliary tip staining is
741 more strong in the triple mutants. Scale bars: 3 μm **G)** Fluorescent images from Kinesin II motor
742 (KAP-1::GFP) revealed that the restricted middle segment localization of KAP-1 remains
743 unchanged in w*dr-31(tm10423);elmd-1;rpi-2* triple mutants. Scale bars: 3 μm **H)** Shown are the

744 drawings of phasmid cilia (PHA/PHB sensory neurons in the tail) in wild type and mutants
745 showing ciliary accumulations.
746
747 **Figure 6: Measurement of anterograde and retrograde IFT transport frequency A)** Shown
748 are representative kymographs of GFP tagged IFT proteins translocating in the tail cilia (PHA/PHB
749 sensory neurons) of wild type and indicated mutants. Kymographs for anterograde, retrogrades
750 and merged (Red & Green) were generated with ImageJ equipped with KymographClear. The
751 trajectory represents a moving IFT particle, and the average number of moving IFT particles in
752 wild type and indicated double and triple mutants was calculated by counting all trajectories in
753 each kymograph. Travel time and distance are shown on kymographs. **B)** Box-and-Whisker charts
754 with error bars were created to visualize the average number of IFT anterograde and retrograde
755 particles between wild type and indicated mutants. The Mann–Whitney U test was used to measure
756 statistical analysis and significance. The four and three asterisks (**** and ***) at the top of the
757 brackets indicate that the p value between the two strains is less than 0.0001 and 0.001,
758 respectively, suggesting statistical significance. Ns stands for "not significant."
759 **Figure 7: The CRISPR/Cas9 knock-in (p.Arg261del) *C. elegans* model of the human patient**
760 **variant phenocopies the cilia related anomalies in the null *wdr-31 C. elegans* mutants. A)**
761 Shown are multiple sequence alignments of WDR31 between human, chimp, macaca, rat and *C.*
762 *elegans.* The arginine residue at 268 was converted to a stop codon (R268*) in the ciliopathy
763 patient, causing the last almost 100 amino acids not to be translated, and the arginine residue at
764 268 of human WDR31 was conserved between humans and other organisms included. To mimic
765 a comparable human patient variant in *C. elegans*, the CRISPR/Cas9 was used to create the
766 deletion starting from the arginine residue at 261 of *C. elegans* WDR-31. **B)** Shown are

767 fluorescence images of WDR-31::GFP and WDR-31($^{R261\text{-}del}$)::GFP with the transition zone marker
768 MKS-6:mCherry in the tail. Both WDR-31 markers are located directly underneath the TZ. **C)**
769 Shown are fluorescence images together with cartoon representations. *wdr-31($^{R261\text{-}del}$);elmd-1;rpi-*
770 *2* triple mutants exhibit dye-filling (Dyf) phenotype. **D)** Fluorescence images and the
771 representative cartons display the fork-like structure of the AWB cilia in wild type and indicated
772 mutant backgrounds. In all examined *wdr-31* triple mutants, including *wdr-31($^{R261\text{-}del}$);elmd-1;rpi-*
773 *2*, the backward projections from the base of AWB cilia were observed. The ectopic projection
774 from the cilia was shown in *wdr-31($^{R261\text{-}del}$);elmd-1* double mutant. Asterisks (*) points the
775 backward projection while p indicates ectopic projections from the middle parts of cilia. **E)** The
776 percentage distribution of AWB cilia morphology in wild type and indicated mutants is displayed
777 in the graph. **F)** Confocal fluorescent images exhibit the localization of tdTomato tagged TRAM-
778 1 (a PCMC marker) and MSK-2::GFP (a TZ marker) in wild type and indicated mutants. TRAM-
779 1 leaks into cilia in all four *wdr-31* triple mutants, including the disease phenocopying mutant.
780 Cilia, PCMC, and TZ are depicted in the fluorescent image. Scale bars: 2 µm
781
782 **Figure 8: WDR-31 and ELMD-1 regulate the recruitment of BBSome to cilia.**
783 **A)** Shown are fluorescence images from the transgenic strain carrying IFT-74::GFP, an IFT-B
784 component, in wild type, *wdr-31;elmd-1* double mutants, *wdr-31;elmd-1;rpi-2* triple mutants, and
785 *bbs-8(nx77).* The IFT-B subunit IFT-74:GFP accumulates at the ciliary tips and cilia in the tail of
786 all three mutants. **B)** Confocal fluorescence images showing the localization of BBS-7:GFP, a
787 BBSome subunit, in the heads and tails of wild type and *wdr-31(tm10423); wdr-31;elmd-1*; *rpi-*
788 *2;elmd-1* double and *wdr-31;elmd-1;rpi-2* triple mutants. Fluorescence images showed absent or
789 weak cilia staining of BBS-7::GFP in both the head and tails of *wdr-31;elmd-1* and *wdr-31;elmd-*

790 *1;rpi-2* triple mutants. **C)** Kymographs were created from time-lapse BBS-7::GFP movies
791 (PHA/PHB cilia) using KymographClear integrated into ImageJ. Shown are representative
792 kymographs for BBS-7::GFP translocating in wild type and indicated mutants. Each trajectory in
793 kymographs was counted. Travel time and distance are included on kymograph **D)** The graph
794 depicts the average number of BBS-7::GFP particles traveling around cilia in both directions for
795 wild type and indicated mutants. The Mann–Whitney U test revealed statistical significance
796 between the compared strains and that the p value was less than 0.0001 shown by the four asterisks
797 (****) at the top of the brackets **E)** In wild type, the assembly of the Kinesin-IFT-BBSome
798 complex (Kinesin-II and OSM-3**,** IFT-B , IFT-A and BBSome) happens at the base of cilia. In the
799 middle segment of amphid and phasmid cilia in *C. elegans*, both heterotrimeric Kinesin II and
800 homodimeric OSM-3 transport the IFT-A- IFT-B- BBSome complex in an anterograde direction.
801 Heterotrimeric Kinesin II returns to the ciliary base when it reaches the tip of the middle segment
802 of amphid and phasmid cilia, whereas homodimeric OSM-3 is responsible for the anterograde
803 translocation of the IFT-BBSome complex in the distal segment of amphid and phasmid cilia.
804 When the OSM-3-IFT-BBSome complex reaches the ciliary tip, cytoplasmic dynein transports
805 them back to the ciliary base. In *wdr-31;elmd-1* double *wdr-31;elmd-1;rpi-2* triple mutants, the
806 BBSome failed to enter into cilia, thus leading to accumulations of OSM-3 and IFT-B components
807 in the ciliary tips.
808
809 **Supplementary Figure 1: Expression patterns of WDR-31 and ELMD-1. A)** A total of 60
810 sensory neurons are distributed in the head (amphid) and tails (phasmid) of *C. elegans.* The ciliated
811 sensory neurons are displayed in the schematic of *C. elegans.* The expression of *elmd-*
812 *1promoter::gfp* (1000 kb) and *wdr-31promoter::gfp* (1000 kb) were shown in the fluorescence

813 images. The cell of ciliated sensory neurons (cell soma) in the head and tails were displayed in
814 brackets.

815 **Supplementary Figure 2: Localization of A)** Images showing immunostaining of a ciliary
816 marker ARL13B and DAPI (nucleus) in hTERT-RPE1 cells. NT represents no transfection of
817 hTERT-RPE1 with WDR31 (tagged with cyan fluorescent protein) and ELMOD3 (tagged with
818 red fluorescent protein). Scale bars: 10 µm. **B)** Images showing immunostaining of hTERT-RPE1
819 cells transfected with ELMOD3-CFP (cyan) and also stained for ARL13B (yellow). The magenta
820 channel only shows some background but no localization to the cilium. Green regions in the
821 "merge" picture show co-localization of both ELMOD3 and ARL13B proteins. Scale bars: 3 µm.
822 **C)** Fluorescence images displaying hTERT-RPE1 Fluorescence images of immunostaining for
823 ARL13B (yellow) and WDR31-RFP (magenta) in hTERT-RPE1 cells transfected with WDR31-
824 RFP (cyan). The cyan channel shows some background, with no cilium localisation. WDR31 and
825 ARL1B proteins are co-localized in the pink sections of the "merge" image. Scale bars: 3 µm.
826

827 **Supplementary Figure 3: Rescue of dye uptake defects by ELMD-1 or RPI-2.**
828 **A)** Shown are representative schematics of human and C. elegans WDR-31/WDR31. Human
829 WDR31 (NP_660284.1) has four WD domains while *C. elegans* WDR-31 (NP_494344.1) has
830 three WD domains (https://prosite.expasy.org/; Sigrist CJA et al 2012). **B)** Schematic diagrams of
831 *wdr-31*, *elmd-1* and *rpi-2* together with corresponding deletions are shown. Scale bars: 250 bp. **C**
832 **and D**) Fluorescence microscope images of mutant worms (head and tail) with red-fluorescent dye
833 uptake (texas red filter) and GFP-tagged ELMD-1 and RPI-2 (fluorescence filter set for GFP) are
834 shown. The head or tail in the dotted lines is indicated by numbers in the combined fluorescence

835 images. GFP expression in combination with RED fluorescence indicates the rescue of dye uptake
836 defects.
837 **Supplementary Figure 4: A)** 100% stacked column chart displays the proportion of *C. elegans*
838 wild type and indicated mutants cross the osmotic barrier containing an 8M fructose solution with
839 bromophenol blue. Stay represents not crossing the osmotic barrier while pass means that animal
840 crossed the osmotic barrier. The number of animals used in osmotic avoidance assays for each
841 strain are shown on the bar charts. **B and C)** The percentage of dye uptake in the head and tail in
842 wild type and mutants, as well as the defect in AWB cilia morphology, are displayed in bar charts.
843 Dyf represents dye uptake defects while the partial means some cells in the head or tail take up the
844 fluorescence dye but others could not fill up their cells. Fisher's exact test was performed for
845 statistical analysis between indicated triple mutants and a rescue gene for Dye assay or wild type
846 and indicated mutants for AWB cilia morphology. Brackets show statistical significance between
847 two strains compared ($p < 0.0001$) in B and **** indicates statistical significance in C. **D)** Shown
848 is the jitter plot for AWB long cilia length (µm) for wild type and indicated mutant strains.
849
850 **Supplementary Figure 5: A)** Shown is the co-localization of WDR-31(R261del)::GFP (a *C.*
851 *elegans* variant mimicking disease-associated human R268* variant) and MKS-6::mCherry
852 (transition zone protein) in the tail (PHA/PHB sensory neuron) of *C. elegans*. Shown is a schematic
853 drawing of the PHA/PHB sensory neuron. CB denotes the cell body. axon dendrite and transition
854 zone are shown in the images and schematic drawing. **B)** Shown is co-localization of RPI-2::GFP
855 (human RP2) and XBX-1::mCherry (human DYNC2LI1) in the head and tail sensory neurons.
856 XBX-1 stains the entire cilium and is used as a ciliary marker while RPI-2 is located at PCMC.
857 PCMC denotes the periciliary membrane compartment.

858

859 **Supplementary Figure 6: A)** Confocal images (Z-stack) display the localization of OSM-6::GFP
860 (a single copy transgene, huma IFT52) in the head (a bunch of cilia) of wild type and indicated
861 mutants. Arrow points the ciliary tips while asterisks indicate the ciliary base. **B, C and D)**
862 Confocal images show colocalization of TAX-4 (a ciliary membrane protein) and XBX-
863 1::tdTomato (a cilia marker) or NPHP-1::GFP (transition zone protein) and FBF-1:: mCherry
864 (transition fiber protein) or PLCδ1-PH::GFP (a marker for monitoring phosphatidylinositol 4,5-
865 bisphosphate (PtdIns(4,5)P2) in the plasma membrane) and MKSR-2 (a TZ marker). The
866 localization of TAX-4::GFP in *wdr-31;elmd-1;rpi-2* triple mutants was similar to wild type. The
867 PLCδ1-PH::GFP decorates the membranes of PCMC and does not enter into cilia in wild type.
868 The PLCδ1-PH::GFP stays outside of cilia in the *wdr-31;elmd-1;rpi-2* triple mutants.

869

870 **Supplementary Movies**

871 For the IFT assay, time-lapse movies (3 frames per second) were generated with Leica DM6, and
872 were processed with Image J to generate GIFs (10 fps).

873 **Supplementary Movies:**

874 **Supplementary Movie 1:** IFT-74::GFP in wild type and indicated mutant backgrounds.

875 **Supplementary Movie 2:** OSM-6::GFP in wild type and indicated mutant backgrounds.

876 **Supplementary Movie 3:** OSM-3::GFP in wild type and indicated mutant backgrounds

877 **Supplementary Movie 4:** GFP::CHE-3 in wild type and indicated mutant backgrounds.

878 **Supplementary Movie 5:** IFT-140::GFP in wild type and indicated mutant backgrounds.

879 **Supplementary Movie 6:** BBS-7::GFP in wild type and indicated mutant backgrounds.

880 **References**

881 Ansley, S.J., Badano, J.L., Blacque, O.E., Hill, J., Hoskins, B.E., Leitch, C.C., Chul Kim, J.,

882 Ross, A.J., Eichers, E.R., Teslovich, T.M., Mah, A.K., Johnsen, R.C., Cavender, J.C.,
883 Alan Lewis, R., Leroux, M.R., Beales, P.L., Katsanis, N., 2003. Basal body dysfunction is
884 a likely cause of pleiotropic Bardet–Biedl syndrome. Nature 425, 628–633.
885 https://doi.org/10.1038/nature02030
886
887 Anvarian, Z., Mykytyn, K., Mukhopadhyay, S., Pedersen, L.B., Christensen, S.T., 2019. Cellular
888 signalling by primary cilia in development, organ function and disease. Nat. Rev.
889 Nephrol. 15, 199–219. https://doi.org/10.1038/s41581-019-0116-9
890
891 Arnaiz, O., Malinowska, A., Klotz, C., Sperling, L., Dadlez, M., Koll, F., Cohen, J., 2009. Cildb: a
892 knowledgebase for centrosomes and cilia. Database 2009.
893 https://doi.org/10.1093/database/bap022
894
895 Avidor-Reiss, T., Maer, A.M., Koundakjian, E., Polyanovsky, A., Keil, T., Subramaniam, S.,
896 Zuker, C.S., 2004. Decoding Cilia Function. Cell 117, 527–539.
897 https://doi.org/10.1016/S0092-8674(04)00412-X
898
899 Blacque, O., E., 2008. Intraflagellar transport: from molecular characterisation to mechanism.
900 Front. Biosci. 13, 2633. https://doi.org/10.2741/2871
901
902 Blacque, O.E., 2004. Loss of C. elegans BBS-7 and BBS-8 protein function results in cilia
903 defects and compromised intraflagellar transport. Genes Dev. 18, 1630–1642.
904 https://doi.org/10.1101/gad.1194004
905
906 Blacque, O.E., Li, C., Inglis, P.N., Esmail, M.A., Ou, G., Mah, A.K., Baillie, D.L., Scholey, J.M.,
907 Leroux, M.R., 2006. The WD Repeat-containing Protein IFTA-1 Is Required for
908 Retrograde Intraflagellar Transport. Mol. Biol. Cell 17, 5053–5062.
909 https://doi.org/10.1091/mbc.e06-06-0571
910
911 Blacque, O.E., Perens, E.A., Boroevich, K.A., Inglis, P.N., Li, C., Warner, A., Khattra, J., Holt,
912 R.A., Ou, G., Mah, A.K., McKay, S.J., Huang, P., Swoboda, P., Jones, S.J.M., Marra,
913 M.A., Baillie, D.L., Moerman, D.G., Shaham, S., Leroux, M.R., 2005. Functional
914 Genomics of the Cilium, a Sensory Organelle. Curr. Biol. 15, 935–941.
915 https://doi.org/10.1016/j.cub.2005.04.059
916
917 Blacque, O.E., Sanders, A.A., 2014. Compartments within a compartment: What *C. elegans* can
918 tell us about ciliary subdomain composition, biogenesis, function, and disease.
919 Organogenesis 10, 126–137. https://doi.org/10.4161/org.28830
920
921 Bloodgood, R.A., 2009. From Central to Rudimentary to Primary: The History of an
922 Underappreciated Organelle Whose Time Has Come.The Primary Cilium, in: Methods in
923 Cell Biology. Elsevier, pp. 2–52. https://doi.org/10.1016/S0091-679X(08)94001-2
924
925 Brenner, S., 1974. The genetics of Caenorhabditis elegans. Genetics 77, 71–94.
926
927 Breslow, D.K., Hoogendoorn, S., Kopp, A.R., Morgens, D.W., Vu, B.K., Kennedy, M.C., Han, K.,
928 Li, A., Hess, G.T., Bassik, M.C., Chen, J.K., Nachury, M.V., 2018. A CRISPR-based
929 screen for Hedgehog signaling provides insights into ciliary function and ciliopathies.
930 Nat. Genet. 50, 460–471. https://doi.org/10.1038/s41588-018-0054-7
931
932 Chang, N., Sun, C., Gao, L., Zhu, D., Xu, X., Zhu, X., Xiong, J.-W., Xi, J.J., 2013. Genome

933 editing with RNA-guided Cas9 nuclease in Zebrafish embryos. Cell Res. 23, 465–472.
934 https://doi.org/10.1038/cr.2013.45
935
936 Choksi, S.P., Babu, D., Lau, D., Yu, X., Roy, S., 2014. Systematic discovery of novel ciliary
937 genes through functional genomics in the zebrafish. Development 141, 3410–3419.
938 https://doi.org/10.1242/dev.108209
939
940 Dickinson, D.J., Ward, J.D., Reiner, D.J., Goldstein, B., 2013. Engineering the Caenorhabditis
941 elegans genome using Cas9-triggered homologous recombination. Nat. Methods 10,
942 1028–1034. https://doi.org/10.1038/nmeth.2641
943
944 Evans, R.J., Schwarz, N., Nagel-Wolfrum, K., Wolfrum, U., Hardcastle, A.J., Cheetham, M.E.,
945 2010. The retinitis pigmentosa protein RP2 links pericentriolar vesicle transport between
946 the Golgi and the primary cilium. Hum. Mol. Genet. 19, 1358–1367.
947 https://doi.org/10.1093/hmg/ddq012
948
949 Gabler, F., Nam, S., Till, S., Mirdita, M., Steinegger, M., Söding, J., Lupas, A.N., Alva, V., 2020.
950 Protein Sequence Analysis Using the MPI Bioinformatics Toolkit. Curr. Protoc.
951 Bioinforma. 72. https://doi.org/10.1002/cpbi.108
952
953 Haycraft, C.J., Swoboda, P., Taulman, P.D., Thomas, J.H., Yoder, B.K., 2001. The C. elegans
954 homolog of the murine cystic kidney disease gene Tg737 functions in a ciliogenic
955 pathway and is disrupted in osm-5 mutant worms. Dev. Camb. Engl. 128, 1493–1505.
956
957 Herman, R.K., Hedgecock, E.M., 1990. Limitation of the size of the vulval primordium of
958 Caenorhabditis elegans by lin-15 expression in surrounding hypodermis. Nature 348,
959 169–171. https://doi.org/10.1038/348169a0
960
961 Ivanova, A.A., East, M.P., Yi, S.L., Kahn, R.A., 2014. Characterization of Recombinant ELMOD
962 (Cell Engulfment and Motility Domain) Proteins as GTPase-activating Proteins (GAPs)
963 for ARF Family GTPases. J. Biol. Chem. 289, 11111–11121.
964 https://doi.org/10.1074/jbc.M114.548529
965
966 Jaworek, T.J., Richard, E.M., Ivanova, A.A., Giese, A.P.J., Choo, D.I., Khan, S.N., Riazuddin,
967 Sheikh, Kahn, R.A., Riazuddin, Saima, 2013. An Alteration in ELMOD3, an Arl2
968 GTPase-Activating Protein, Is Associated with Hearing Impairment in Humans. PLoS
969 Genet. 9, e1003774. https://doi.org/10.1371/journal.pgen.1003774
970
971 Jensen, V.L., Carter, S., Sanders, A.A.W.M., Li, C., Kennedy, J., Timbers, T.A., Cai, J.,
972 Scheidel, N., Kennedy, B.N., Morin, R.D., Leroux, M.R., Blacque, O.E., 2016. Whole-
973 Organism Developmental Expression Profiling Identifies RAB-28 as a Novel Ciliary
974 GTPase Associated with the BBSome and Intraflagellar Transport. PLOS Genet. 12,
975 e1006469. https://doi.org/10.1371/journal.pgen.1006469
976
977 Jin, H., White, S.R., Shida, T., Schulz, S., Aguiar, M., Gygi, S.P., Bazan, J.F., Nachury, M.V.,
978 2010. The Conserved Bardet-Biedl Syndrome Proteins Assemble a Coat that Traffics
979 Membrane Proteins to Cilia. Cell 141, 1208–1219.
980 https://doi.org/10.1016/j.cell.2010.05.015
981
982 Johnson, K.R., Longo-Guess, C.M., Gagnon, L.H., 2012. Mutations of the Mouse ELMO
983 Domain Containing 1 Gene (Elmod1) Link Small GTPase Signaling to Actin

Cytoskeleton Dynamics in Hair Cell Stereocilia. PLoS ONE 7, e36074. https://doi.org/10.1371/journal.pone.0036074

Kaplan, O.I., Doroquez, D.B., Cevik, S., Bowie, R.V., Clarke, L., Sanders, A.A.W.M., Kida, K., Rappoport, J.Z., Sengupta, P., Blacque, O.E., 2012. Endocytosis Genes Facilitate Protein and Membrane Transport in C. elegans Sensory Cilia. Curr. Biol. 22, 451–460. https://doi.org/10.1016/j.cub.2012.01.060

Lambacher, N.J., Bruel, A.-L., van Dam, T.J.P., Szymańska, K., Slaats, G.G., Kuhns, S., McManus, G.J., Kennedy, J.E., Gaff, K., Wu, K.M., van der Lee, R., Burglen, L., Doummar, D., Rivière, J.-B., Faivre, L., Attié-Bitach, T., Saunier, S., Curd, A., Peckham, M., Giles, R.H., Johnson, C.A., Huynen, M.A., Thauvin-Robinet, C., Blacque, O.E., 2016. TMEM107 recruits ciliopathy proteins to subdomains of the ciliary transition zone and causes Joubert syndrome. Nat. Cell Biol. 18, 122–131. https://doi.org/10.1038/ncb3273

Lechtreck, K.-F., Johnson, E.C., Sakai, T., Cochran, D., Ballif, B.A., Rush, J., Pazour, G.J., Ikebe, M., Witman, G.B., 2009. The Chlamydomonas reinhardtii BBSome is an IFT cargo required for export of specific signaling proteins from flagella. J. Cell Biol. 187, 1117–1132. https://doi.org/10.1083/jcb.200909183

Lee, E., Sivan-Loukianova, E., Eberl, D.F., Kernan, M.J., 2008. An IFT-A protein is required to delimit functionally distinct zones in mechanosensory cilia. Curr. Biol. CB 18, 1899–1906. https://doi.org/10.1016/j.cub.2008.11.020

Li, J.B., Gerdes, J.M., Haycraft, C.J., Fan, Y., Teslovich, T.M., May-Simera, H., Li, H., Blacque, O.E., Li, L., Leitch, C.C., Lewis, R.A., Green, J.S., Parfrey, P.S., Leroux, M.R., Davidson, W.S., Beales, P.L., Guay-Woodford, L.M., Yoder, B.K., Stormo, G.D., Katsanis, N., Dutcher, S.K., 2004. Comparative Genomics Identifies a Flagellar and Basal Body Proteome that Includes the BBS5 Human Disease Gene. Cell 117, 541–552. https://doi.org/10.1016/S0092-8674(04)00450-7

Liem, K.F., Ashe, A., He, M., Satir, P., Moran, J., Beier, D., Wicking, C., Anderson, K.V., 2012. The IFT-A complex regulates Shh signaling through cilia structure and membrane protein trafficking. J. Cell Biol. 197, 789–800. https://doi.org/10.1083/jcb.201110049

Loktev, A.V., Zhang, Q., Beck, J.S., Searby, C.C., Scheetz, T.E., Bazan, J.F., Slusarski, D.C., Sheffield, V.C., Jackson, P.K., Nachury, M.V., 2008. A BBSome Subunit Links Ciliogenesis, Microtubule Stability, and Acetylation. Dev. Cell 15, 854–865. https://doi.org/10.1016/j.devcel.2008.11.001

Mangeol, P., Prevo, B., Peterman, E.J.G., 2016. KymographClear and KymographDirect: two tools for the automated quantitative analysis of molecular and cellular dynamics using kymographs. Mol. Biol. Cell 27, 1948–1957. https://doi.org/10.1091/mbc.E15-06-0404

Mick, D.U., Rodrigues, R.B., Leib, R.D., Adams, C.M., Chien, A.S., Gygi, S.P., Nachury, M.V., 2015. Proteomics of Primary Cilia by Proximity Labeling. Dev. Cell 35, 497–512. https://doi.org/10.1016/j.devcel.2015.10.015

Miryounesi, M., Bahari, S., Salehpour, S., Alipour, N., Ghafouri-Fard, S., 2019. ELMO Domain Containing 1 (ELMOD1) Gene Mutation Is Associated with Mental Retardation and Autism Spectrum Disorder. J. Mol. Neurosci. 69, 312–315.

https://doi.org/10.1007/s12031-019-01359-z

Mukhopadhyay, S., Wen, X., Chih, B., Nelson, C.D., Lane, W.S., Scales, S.J., Jackson, P.K., 2010. TULP3 bridges the IFT-A complex and membrane phosphoinositides to promote trafficking of G protein-coupled receptors into primary cilia. Genes Dev. 24, 2180–2193. https://doi.org/10.1101/gad.1966210

Nachury, M.V., 2014. How do cilia organize signalling cascades? Philos. Trans. R. Soc. Lond. B. Biol. Sci. 369. https://doi.org/10.1098/rstb.2013.0465

Nachury, M.V., Loktev, A.V., Zhang, Q., Westlake, C.J., Peränen, J., Merdes, A., Slusarski, D.C., Scheller, R.H., Bazan, J.F., Sheffield, V.C., Jackson, P.K., 2007. A Core Complex of BBS Proteins Cooperates with the GTPase Rab8 to Promote Ciliary Membrane Biogenesis. Cell 129, 1201–1213. https://doi.org/10.1016/j.cell.2007.03.053

Nozaki, S., Castro Araya, R.F., Katoh, Y., Nakayama, K., 2019. Requirement of IFT-B–BBSome complex interaction in export of GPR161 from cilia. Biol. Open 8, bio043786. https://doi.org/10.1242/bio.043786

Ou, G., E. Blacque, O., Snow, J.J., Leroux, M.R., Scholey, J.M., 2005. Functional coordination of intraflagellar transport motors. Nature 436, 583–587. https://doi.org/10.1038/nature03818

Ou, G., Koga, M., Blacque, O.E., Murayama, T., Ohshima, Y., Schafer, J.C., Li, C., Yoder, B.K., Leroux, M.R., Scholey, J.M., 2007. Sensory Ciliogenesis in *Caenorhabditis elegans* : Assignment of IFT Components into Distinct Modules Based on Transport and Phenotypic Profiles. Mol. Biol. Cell 18, 1554–1569. https://doi.org/10.1091/mbc.e06-09-0805

Patel-King, R.S., Gilberti, R.M., Hom, E.F.Y., King, S.M., 2013. WD60/FAP163 is a dynein intermediate chain required for retrograde intraflagellar transport in cilia. Mol. Biol. Cell 24, 2668–2677. https://doi.org/10.1091/mbc.E13-05-0266

Pazour, G.J., Dickert, B.L., Vucica, Y., Seeley, E.S., Rosenbaum, J.L., Witman, G.B., Cole, D.G., 2000. Chlamydomonas IFT88 and its mouse homologue, polycystic kidney disease gene tg737, are required for assembly of cilia and flagella. J. Cell Biol. 151, 709–718. https://doi.org/10.1083/jcb.151.3.709

Piasecki, B.P., Burghoorn, J., Swoboda, P., 2010. Regulatory Factor X (RFX)-mediated transcriptional rewiring of ciliary genes in animals. Proc. Natl. Acad. Sci. 107, 12969–12974. https://doi.org/10.1073/pnas.0914241107

Prevo, B., Scholey, J.M., Peterman, E.J.G., 2017. Intraflagellar transport: mechanisms of motor action, cooperation, and cargo delivery. FEBS J. 284, 2905–2931. https://doi.org/10.1111/febs.14068

Reiter, J.F., Leroux, M.R., 2017. Genes and molecular pathways underpinning ciliopathies. Nat. Rev. Mol. Cell Biol. 18, 533–547. https://doi.org/10.1038/nrm.2017.60

Richards, S., Aziz, N., Bale, S., Bick, D., Das, S., Gastier-Foster, J., Grody, W.W., Hegde, M.,

1085 Lyon, E., Spector, E., Voelkerding, K., Rehm, H.L., ACMG Laboratory Quality
1086 Assurance Committee, 2015. Standards and guidelines for the interpretation of sequence
1087 variants: a joint consensus recommendation of the American College of Medical Genetics
1088 and Genomics and the Association for Molecular Pathology. Genet. Med. Off. J. Am.
1089 Coll. Med. Genet. 17, 405–424. https://doi.org/10.1038/gim.2015.30
1090
1091 Rompolas, P., Pedersen, L.B., Patel-King, R.S., King, S.M., 2007. *Chlamydomonas* FAP133 is
1092 a dynein intermediate chain associated with the retrograde intraflagellar transport motor.
1093 J. Cell Sci. 120, 3653–3665. https://doi.org/10.1242/jcs.012773
1094
1095 Rosenbaum, J.L., Witman, G.B., 2002. Intraflagellar transport. Nat. Rev. Mol. Cell Biol. 3, 813–
1096 825. https://doi.org/10.1038/nrm952
1097
1098 Ruiz García, S., Deprez, M., Lebrigand, K., Cavard, A., Paquet, A., Arguel, M.-J., Magnone, V.,
1099 Truchi, M., Caballero, I., Leroy, S., Marquette, C.-H., Marcet, B., Barbry, P., Zaragosi, L.-
1100 E., 2019. Novel dynamics of human mucociliary differentiation revealed by single-cell
1101 RNA sequencing of nasal epithelial cultures. Development dev.177428.
1102 https://doi.org/10.1242/dev.177428
1103
1104 Satir, P., Christensen, S.T., 2007. Overview of Structure and Function of Mammalian Cilia.
1105 Annu. Rev. Physiol. 69, 377–400.
1106 https://doi.org/10.1146/annurev.physiol.69.040705.141236
1107
1108 Saudi Mendeliome Group, 2015. Comprehensive gene panels provide advantages over clinical
1109 exome sequencing for Mendelian diseases. Genome Biol. 16, 134.
1110 https://doi.org/10.1186/s13059-015-0693-2
1111
1112 Schneider, C.A., Rasband, W.S., Eliceiri, K.W., 2012. NIH Image to ImageJ: 25 years of image
1113 analysis. Nat. Methods 9, 671–675. https://doi.org/10.1038/nmeth.2089
1114
1115 Scholey, J., 2007. The sensory cilia of Caenorhabditis elegans_Revised. WormBook.
1116 https://doi.org/10.1895/wormbook.1.126.2
1117
1118 Schwarz, N., Lane, A., Jovanovic, K., Parfitt, D.A., Aguila, M., Thompson, C.L., da Cruz, L.,
1119 Coffey, P.J., Chapple, J.P., Hardcastle, A.J., Cheetham, M.E., 2017. Arl3 and RP2
1120 regulate the trafficking of ciliary tip kinesins. Hum. Mol. Genet. 26, 2480–2492.
1121 https://doi.org/10.1093/hmg/ddx143
1122
1123 Shaheen, R., Szymanska, K., Basu, B., Patel, N., Ewida, N., Faqeih, E., Al Hashem, A., Derar,
1124 N., Alsharif, H., Aldahmesh, M.A., Alazami, A.M., Hashem, M., Ibrahim, N., Abdulwahab,
1125 F.M., Sonbul, R., Alkuraya, H., Alnemer, M., Al Tala, S., Al-Husain, M., Morsy, H.,
1126 Seidahmed, M.Z., Meriki, N., Al-Owain, M., AlShahwan, S., Tabarki, B., Salih, M.A.,
1127 Ciliopathy WorkingGroup, Faquih, T., El-Kalioby, M., Ueffing, M., Boldt, K., Logan, C.V.,
1128 Parry, D.A., Al Tassan, N., Monies, D., Megarbane, A., Abouelhoda, M., Halees, A.,
1129 Johnson, C.A., Alkuraya, F.S., 2016. Characterizing the morbid genome of ciliopathies.
1130 Genome Biol. 17, 242. https://doi.org/10.1186/s13059-016-1099-5
1131
1132 Shamseldin, H.E., Shaheen, R., Ewida, N., Bubshait, D.K., Alkuraya, H., Almardawi, E.,
1133 Howaidi, A., Sabr, Y., Abdalla, E.M., Alfaifi, A.Y., Alghamdi, J.M., Alsagheir, A., Alfares,
1134 A., Morsy, H., Hussein, M.H., Al-Muhaizea, M.A., Shagrani, M., Al Sabban, E., Salih,

M.A., Meriki, N., Khan, R., Almugbel, M., Qari, A., Tulba, M., Mahnashi, M., Alhazmi, K., Alsalamah, A.K., Nowilaty, S.R., Alhashem, A., Hashem, M., Abdulwahab, F., Ibrahim, N., Alshidi, T., AlObeid, E., Alenazi, M.M., Alzaidan, H., Rahbeeni, Z., Al-Owain, M., Sogaty, S., Seidahmed, M.Z., Alkuraya, F.S., 2020. The morbid genome of ciliopathies: an update. Genet. Med. Off. J. Am. Coll. Med. Genet. 22, 1051–1060. https://doi.org/10.1038/s41436-020-0761-1

Sigg, M.A., Menchen, T., Lee, C., Johnson, J., Jungnickel, M.K., Choksi, S.P., Garcia, G., Busengdal, H., Dougherty, G.W., Pennekamp, P., Werner, C., Rentzsch, F., Florman, H.M., Krogan, N., Wallingford, J.B., Omran, H., Reiter, J.F., 2017. Evolutionary Proteomics Uncovers Ancient Associations of Cilia with Signaling Pathways. Dev. Cell 43, 744-762.e11. https://doi.org/10.1016/j.devcel.2017.11.014

Silflow, C.D., Lefebvre, P.A., 2001. Assembly and Motility of Eukaryotic Cilia and Flagella. Lessons from *Chlamydomonas reinhardtii*. Plant Physiol. 127, 1500–1507. https://doi.org/10.1104/pp.010807

Sleigh, M.A., 1989. Adaptations of ciliary systems for the propulsion of water and mucus. Comp. Biochem. Physiol. A Physiol. 94, 359–364. https://doi.org/10.1016/0300-9629(89)90559-8

SYSCILIA Study Group, van Dam, T.J., Wheway, G., Slaats, G.G., Huynen, M.A., Giles, R.H., 2013. The SYSCILIA gold standard (SCGSv1) of known ciliary components and its applications within a systems biology consortium. Cilia 2, 7. https://doi.org/10.1186/2046-2530-2-7

Thisse, B., Heyer, V., Lux, A., Alunni, V., Degrave, A., Seiliez, I., Kirchner, J., Parkhill, J.-P., Thisse, C., 2004. Spatial and Temporal Expression of the Zebrafish Genome by Large-Scale In Situ Hybridization Screening, in: Methods in Cell Biology. Elsevier, pp. 505–519. https://doi.org/10.1016/S0091-679X(04)77027-2

Turn, R.E., Linnert, J., Gigante, E.D., Wolfrum, U., Caspary, T., Kahn, R.A., 2021. Roles for ELMOD2 and Rootletin in ciliogenesis. Mol. Biol. Cell 32, 800–822. https://doi.org/10.1091/mbc.E20-10-0635

UK10K Rare Diseases Group, Boldt, K., van Reeuwijk, J., Lu, Q., Koutroumpas, K., Nguyen, T.-M.T., Texier, Y., van Beersum, S.E.C., Horn, N., Willer, J.R., Mans, D.A., Dougherty, G., Lamers, I.J.C., Coene, K.L.M., Arts, H.H., Betts, M.J., Beyer, T., Bolat, E., Gloeckner, C.J., Haidari, K., Hetterschijt, L., Iaconis, D., Jenkins, D., Klose, F., Knapp, B., Latour, B., Letteboer, S.J.F., Marcelis, C.L., Mitic, D., Morleo, M., Oud, M.M., Riemersma, M., Rix, S., Terhal, P.A., Toedt, G., van Dam, T.J.P., de Vrieze, E., Wissinger, Y., Wu, K.M., Apic, G., Beales, P.L., Blacque, O.E., Gibson, T.J., Huynen, M.A., Katsanis, N., Kremer, H., Omran, H., van Wijk, E., Wolfrum, U., Kepes, F., Davis, E.E., Franco, B., Giles, R.H., Ueffing, M., Russell, R.B., Roepman, R., 2016. An organelle-specific protein landscape identifies novel diseases and molecular mechanisms. Nat. Commun. 7, 11491. https://doi.org/10.1038/ncomms11491

van Dam, T.J.P., Kennedy, J., van der Lee, R., de Vrieze, E., Wunderlich, K.A., Rix, S., Dougherty, G.W., Lambacher, N.J., Li, C., Jensen, V.L., Leroux, M.R., Hjeij, R., Horn, N., Texier, Y., Wissinger, Y., van Reeuwijk, J., Wheway, G., Knapp, B., Scheel, J.F., Franco, B., Mans, D.A., van Wijk, E., Képès, F., Slaats, G.G., Toedt, G., Kremer, H.,

1186 Omran, H., Szymanska, K., Koutroumpas, K., Ueffing, M., Nguyen, T.-M.T., Letteboer,
1187 S.J.F., Oud, M.M., van Beersum, S.E.C., Schmidts, M., Beales, P.L., Lu, Q., Giles, R.H.,
1188 Szklarczyk, R., Russell, R.B., Gibson, T.J., Johnson, C.A., Blacque, O.E., Wolfrum, U.,
1189 Boldt, K., Roepman, R., Hernandez-Hernandez, V., Huynen, M.A., 2019. CiliaCarta: An
1190 integrated and validated compendium of ciliary genes. PLOS ONE 14, e0216705.
1191 https://doi.org/10.1371/journal.pone.0216705
1192
1193 Wei, Q., Xu, Q., Zhang, Y., Li, Y., Zhang, Q., Hu, Z., Harris, P.C., Torres, V.E., Ling, K., Hu, J.,
1194 2013. Transition fibre protein FBF1 is required for the ciliary entry of assembled
1195 intraflagellar transport complexes. Nat. Commun. 4, 2750.
1196 https://doi.org/10.1038/ncomms3750
1197
1198 Wei, Q., Zhang, Y., Li, Y., Zhang, Q., Ling, K., Hu, J., 2012. The BBSome controls IFT assembly
1199 and turnaround in cilia. Nat. Cell Biol. 14, 950–957. https://doi.org/10.1038/ncb2560
1200
1201 Wheway, G., Genomics England Research Consortium, Mitchison, H.M., 2019. Opportunities
1202 and Challenges for Molecular Understanding of Ciliopathies–The 100,000 Genomes
1203 Project. Front. Genet. 10, 127. https://doi.org/10.3389/fgene.2019.00127
1204
1205 Williams, C.L., Li, C., Kida, K., Inglis, P.N., Mohan, S., Semenec, L., Bialas, N.J., Stupay, R.M.,
1206 Chen, N., Blacque, O.E., Yoder, B.K., Leroux, M.R., 2011. MKS and NPHP modules
1207 cooperate to establish basal body/transition zone membrane associations and ciliary
1208 gate function during ciliogenesis. J. Cell Biol. 192, 1023–1041.
1209 https://doi.org/10.1083/jcb.201012116
1210
1211 Williams, C.L., McIntyre, J.C., Norris, S.R., Jenkins, P.M., Zhang, L., Pei, Q., Verhey, K.,
1212 Martens, J.R., 2014. Direct evidence for BBSome-associated intraflagellar transport
1213 reveals distinct properties of native mammalian cilia. Nat. Commun. 5, 5813.
1214 https://doi.org/10.1038/ncomms6813
1215
1216 Wright, K.J., Baye, L.M., Olivier-Mason, A., Mukhopadhyay, S., Sang, L., Kwong, M., Wang, W.,
1217 Pretorius, P.R., Sheffield, V.C., Sengupta, P., Slusarski, D.C., Jackson, P.K., 2011. An
1218 ARL3-UNC119-RP2 GTPase cycle targets myristoylated NPHP3 to the primary cilium.
1219 Genes Dev. 25, 2347–2360. https://doi.org/10.1101/gad.173443.111
1220
1221 Xu, Q., Zhang, Y., Wei, Q., Huang, Y., Li, Y., Ling, K., Hu, J., 2015. BBS4 and BBS5 show
1222 functional redundancy in the BBSome to regulate the degradative sorting of ciliary
1223 sensory receptors. Sci. Rep. 5, 11855. https://doi.org/10.1038/srep11855
1224
1225 Xu, W., Jin, M., Hu, R., Wang, H., Zhang, F., Yuan, S., Cao, Y., 2017. The Joubert Syndrome
1226 Protein Inpp5e Controls Ciliogenesis by Regulating Phosphoinositides at the Apical
1227 Membrane. J. Am. Soc. Nephrol. 28, 118–129. https://doi.org/10.1681/ASN.2015080906
1228
1229 Ye, F., Nager, A.R., Nachury, M.V., 2018. BBSome trains remove activated GPCRs from cilia by
1230 enabling passage through the transition zone. J. Cell Biol. 217, 1847–1868.
1231 https://doi.org/10.1083/jcb.201709041

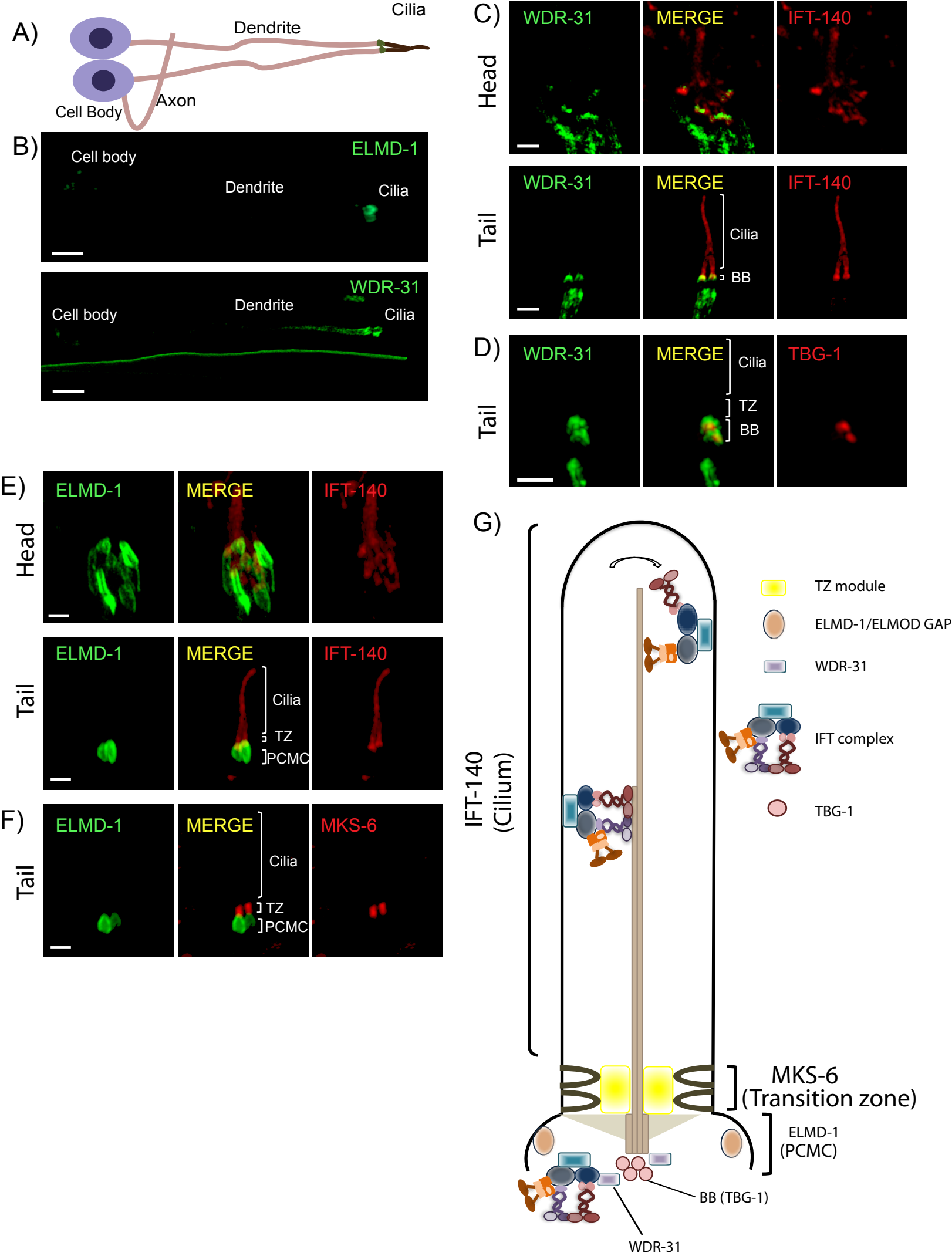
A)
Cilia
Dendrite
Cell Body
Axon
B)
Cell body
ELMD-1
Dendrite
Cilia
Cell body
WDR-31
Dendrite
Cilia
C)
Head
WDR-31
MERGE
IFT-140
Tail
WDR-31
MERGE
IFT-140
Cilia
BB
D)
Tail
WDR-31
MERGE
TBG-1
Cilia
TZ
BB
E)
Head
ELMD-1
MERGE
IFT-140
Tail
ELMD-1
MERGE
IFT-140
Cilia
TZ
PCMC
F)
Tail
ELMD-1
MERGE
MKS-6
Cilia
TZ
PCMC
G)
IFT-140
(Cilium)
TZ module
ELMD-1/ELMOD GAP
WDR-31
IFT complex
TBG-1
MKS-6
(Transition zone)
ELMD-1
(PCMC)
BB (TBG-1)
WDR-31

A)

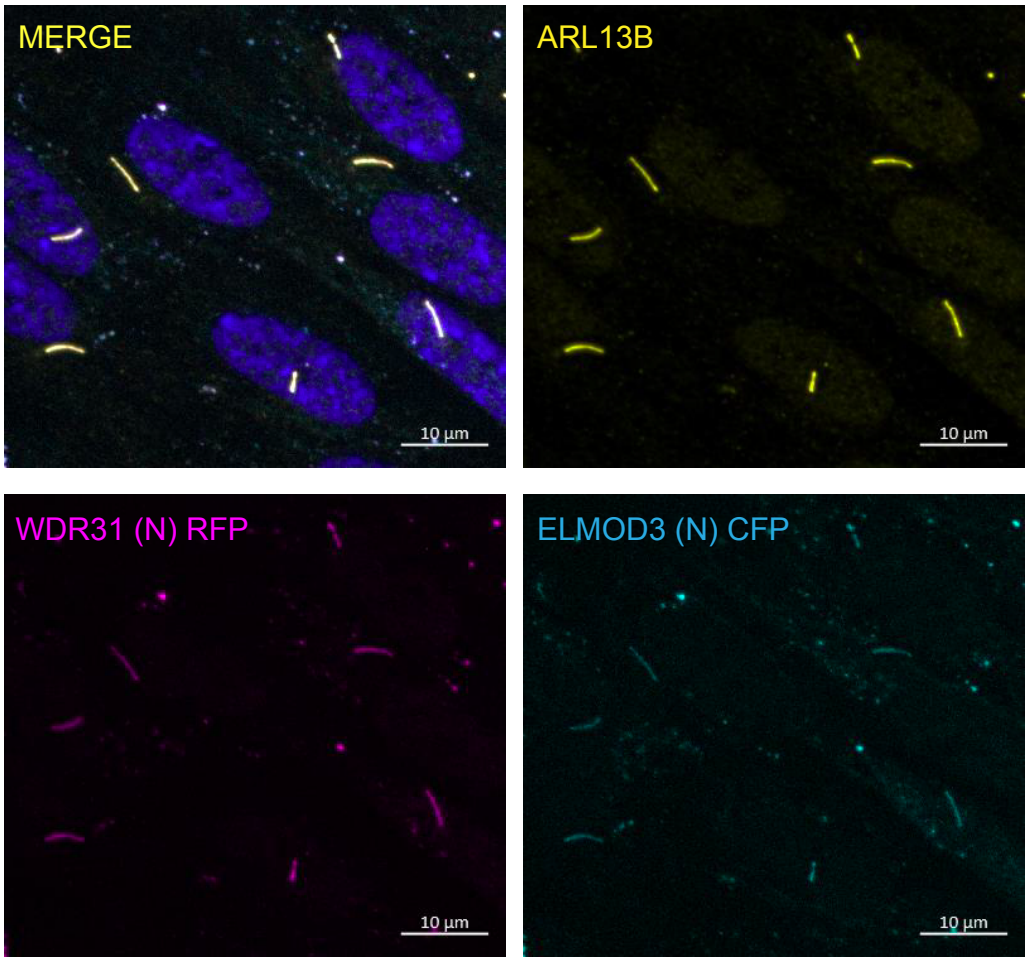
MERGE
10 µm
ARL13B
10 µm
WDR31 (N) RFP
10 µm
ELMOD3 (N) CFP
10 µm

B)

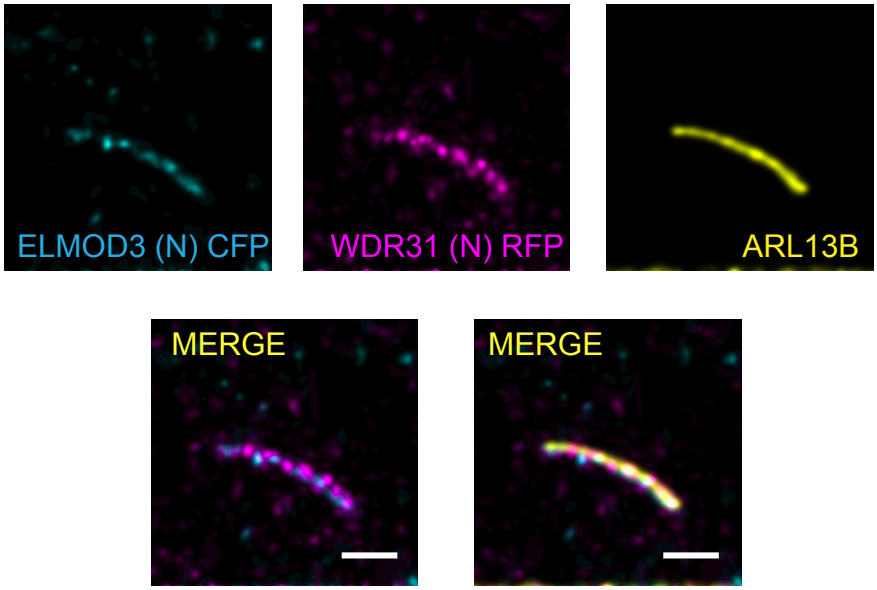
ELMOD3 (N) CFP
WDR31 (N) RFP
ARL13B
MERGE
MERGE

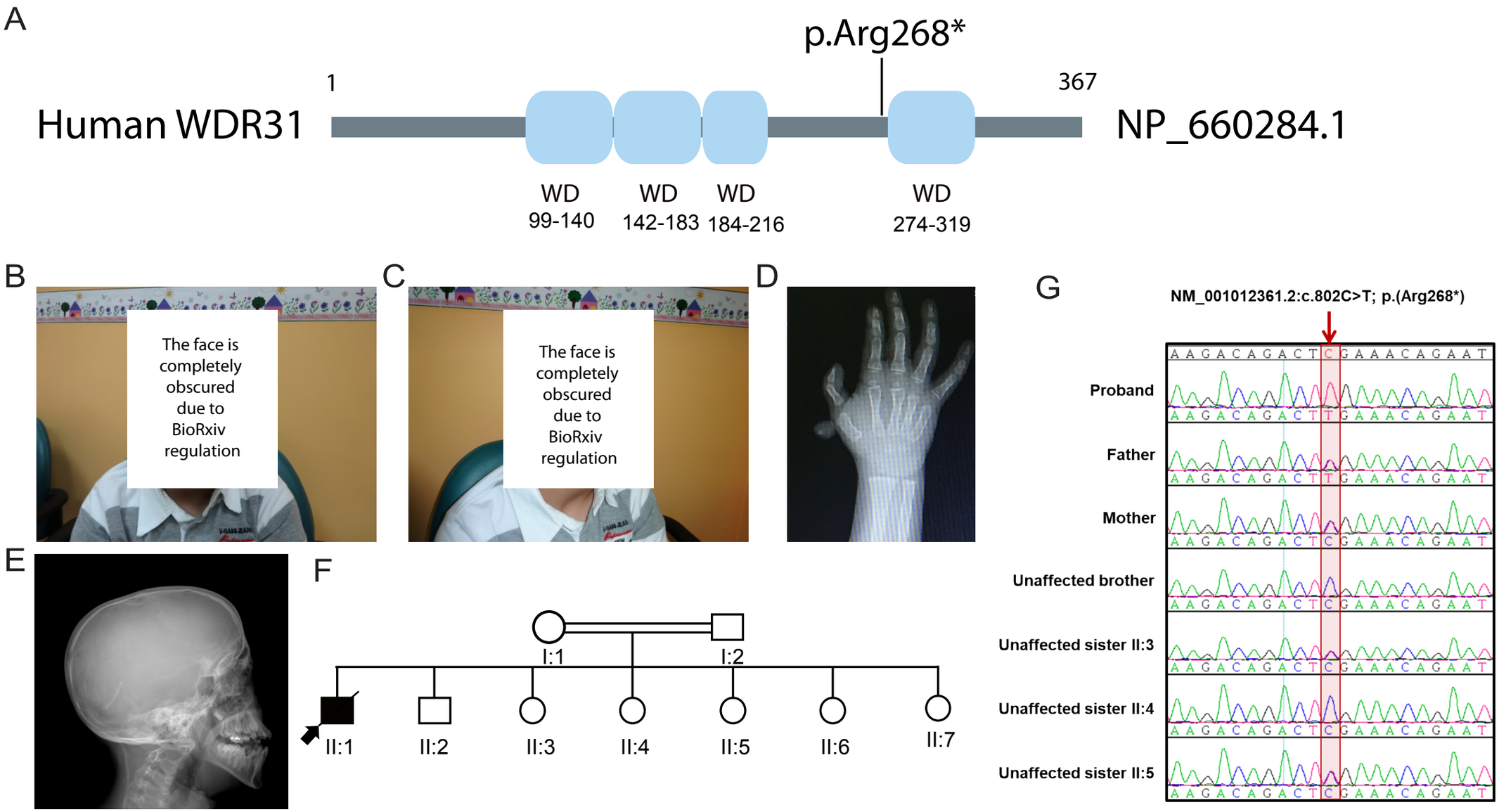
A
p.Arg268*
1
367
Human WDR31
NP_660284.1
WD 99-140
WD 142-183
WD 184-216
WD 274-319
B
The face is completely obscured due to BioRxiv regulation
C
The face is completely obscured due to BioRxiv regulation
D
E
F
I:1
I:2
II:1
II:2
II:3
II:4
II:5
II:6
II:7
G
NM_001012361.2:c.802C>T; p.(Arg268*)
Proband
Father
Mother
Unaffected brother
Unaffected sister II:3
Unaffected sister II:4
Unaffected sister II:5

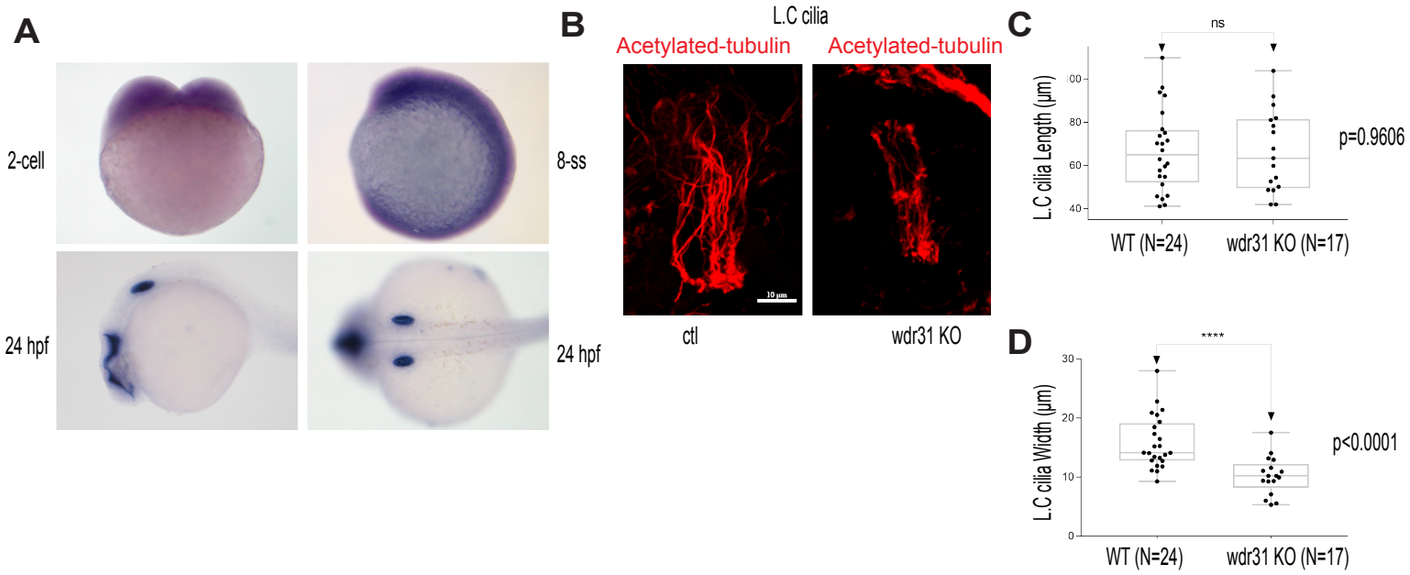
A
2-cell
8-ss
24 hpf
24 hpf
B
L.C cilia
Acetylated-tubulin
Acetylated-tubulin
10 µm
ctl
wdr31 KO
C
ns
L.C cilia Length (µm)
p=0.9606
WT (N=24)
wdr31 KO (N=17)
D
****
L.C cilia Width (µm)
p<0.0001
WT (N=24)
wdr31 KO (N=17)

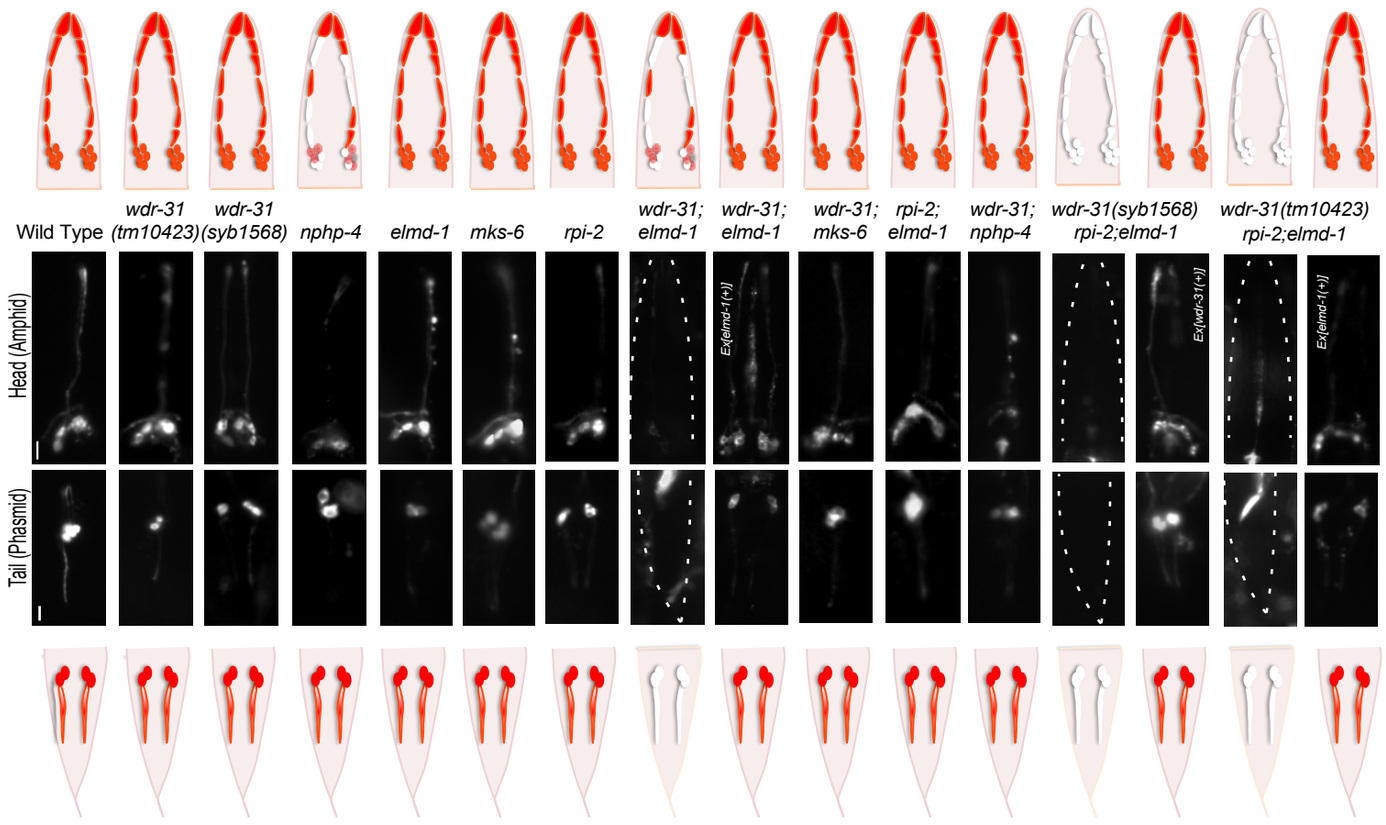
E
Wild Type
wdr-31 (tm10423)
wdr-31 (syb1568)
nphp-4
elmd-1
mks-6
rpi-2
wdr-31; elmd-1
wdr-31; elmd-1
wdr-31; mks-6
rpi-2; elmd-1
wdr-31; nphp-4
wdr-31(syb1568) rpi-2;elmd-1
wdr-31(tm10423) rpi-2;elmd-1
Ex[elmd-1(+)]
Ex[wdr-31(+)]
Ex[elmd-1(+)]
Head (Amphid)
Tail (Phasmid)

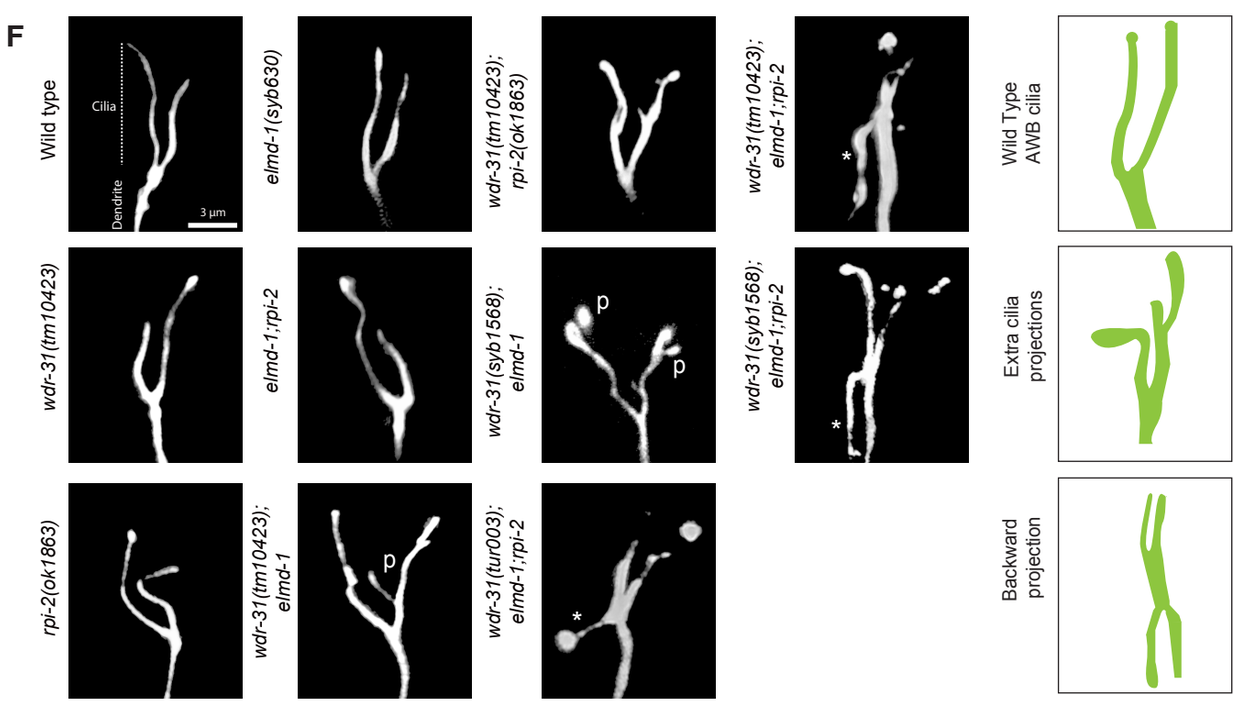
F
Wild type
Cilia
Dendrite
3 µm
elmd-1(syb630)
wdr-31(tm10423); rpi-2(ok1863)
wdr-31(tm10423); elmd-1;rpi-2
Wild Type AWB cilia
wdr-31(tm10423)
elmd-1;rpi-2
wdr-31(syb1568); elmd-1
p
p
wdr-31(syb1568); elmd-1;rpi-2
Extra cilia projections
rpi-2(ok1863)
wdr-31(tm10423); elmd-1
p
wdr-31(tur003); elmd-1;rpi-2
Backward projection

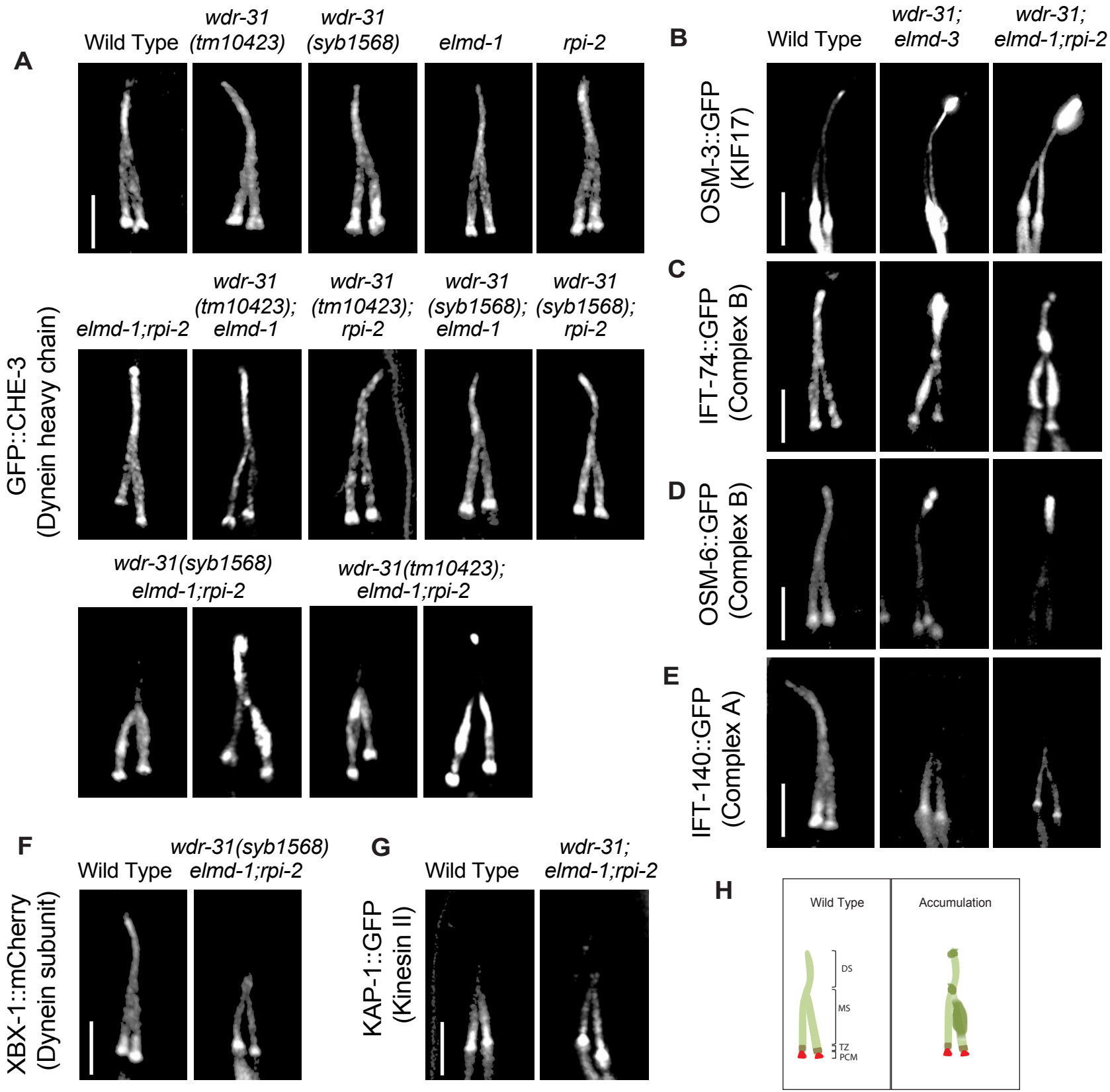
A
Wild Type
wdr-31 (tm10423)
wdr-31 (syb1568)
elmd-1
rpi-2
GFP::CHE-3 (Dynein heavy chain)
elmd-1;rpi-2
wdr-31 (tm10423); elmd-1
wdr-31 (tm10423); rpi-2
wdr-31 (syb1568); elmd-1
wdr-31 (syb1568); rpi-2
wdr-31(syb1568) elmd-1;rpi-2
wdr-31(tm10423); elmd-1;rpi-2
B
Wild Type
wdr-31; elmd-3
wdr-31; elmd-1;rpi-2
OSM-3::GFP (KIF17)
C
IFT-74::GFP (Complex B)
D
OSM-6::GFP (Complex B)
E
IFT-140::GFP (Complex A)
F
Wild Type
wdr-31(syb1568) elmd-1;rpi-2
XBX-1::mCherry (Dynein subunit)
G
Wild Type
wdr-31; elmd-1;rpi-2
KAP-1::GFP (Kinesin II)
H
Wild Type
Accumulation
DS
MS
TZ
PCM

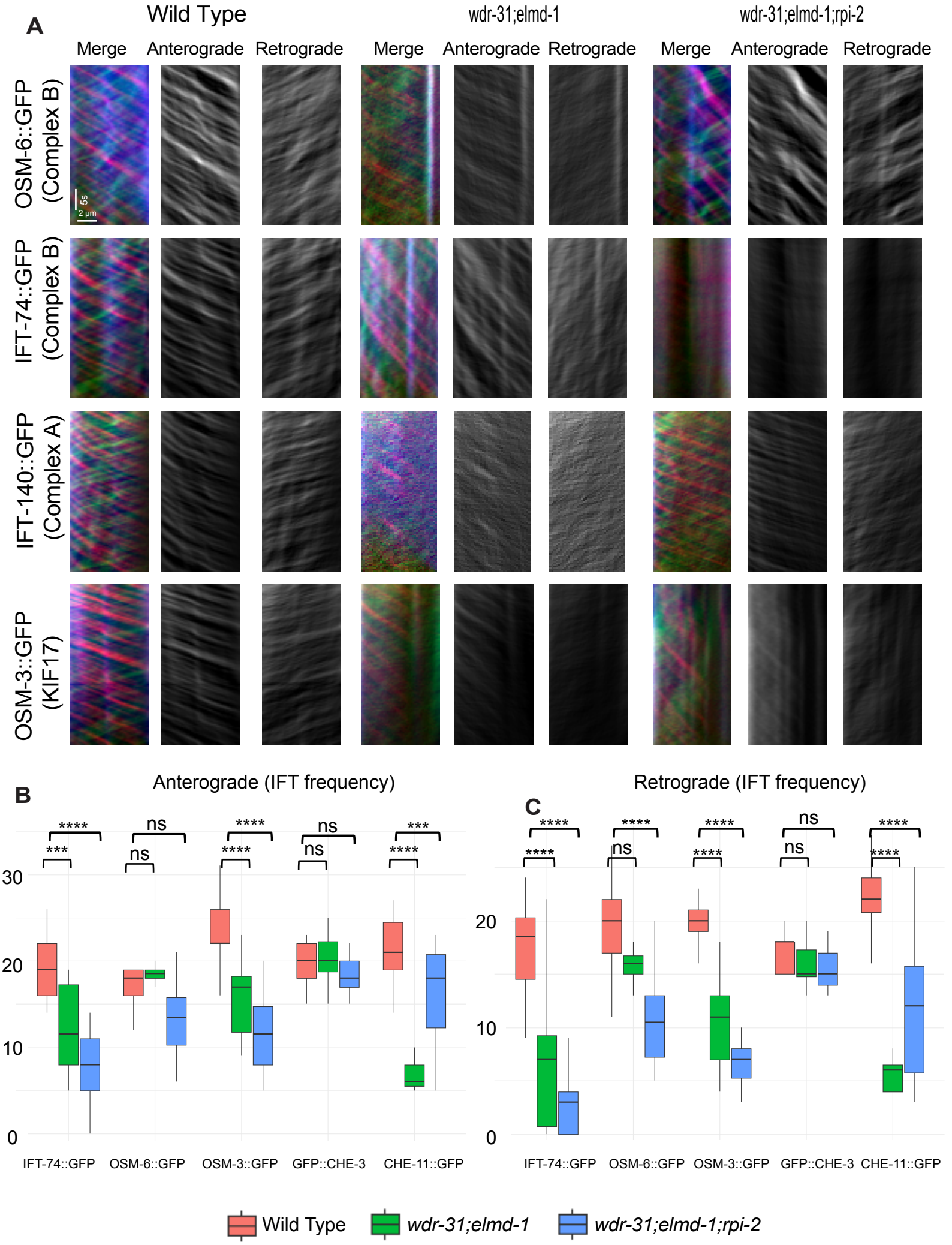
A
Wild Type
wdr-31;elmd-1
wdr-31;elmd-1;rpi-2
Merge
Anterograde
Retrograde
OSM-6::GFP (Complex B)
IFT-74::GFP (Complex B)
IFT-140::GFP (Complex A)
OSM-3::GFP (KIF17)
5s
2 µm
B
Anterograde (IFT frequency)
C
Retrograde (IFT frequency)
****
***
ns
IFT-74::GFP
OSM-6::GFP
OSM-3::GFP
GFP::CHE-3
CHE-11::GFP
Wild Type
wdr-31;elmd-1
wdr-31;elmd-1;rpi-2

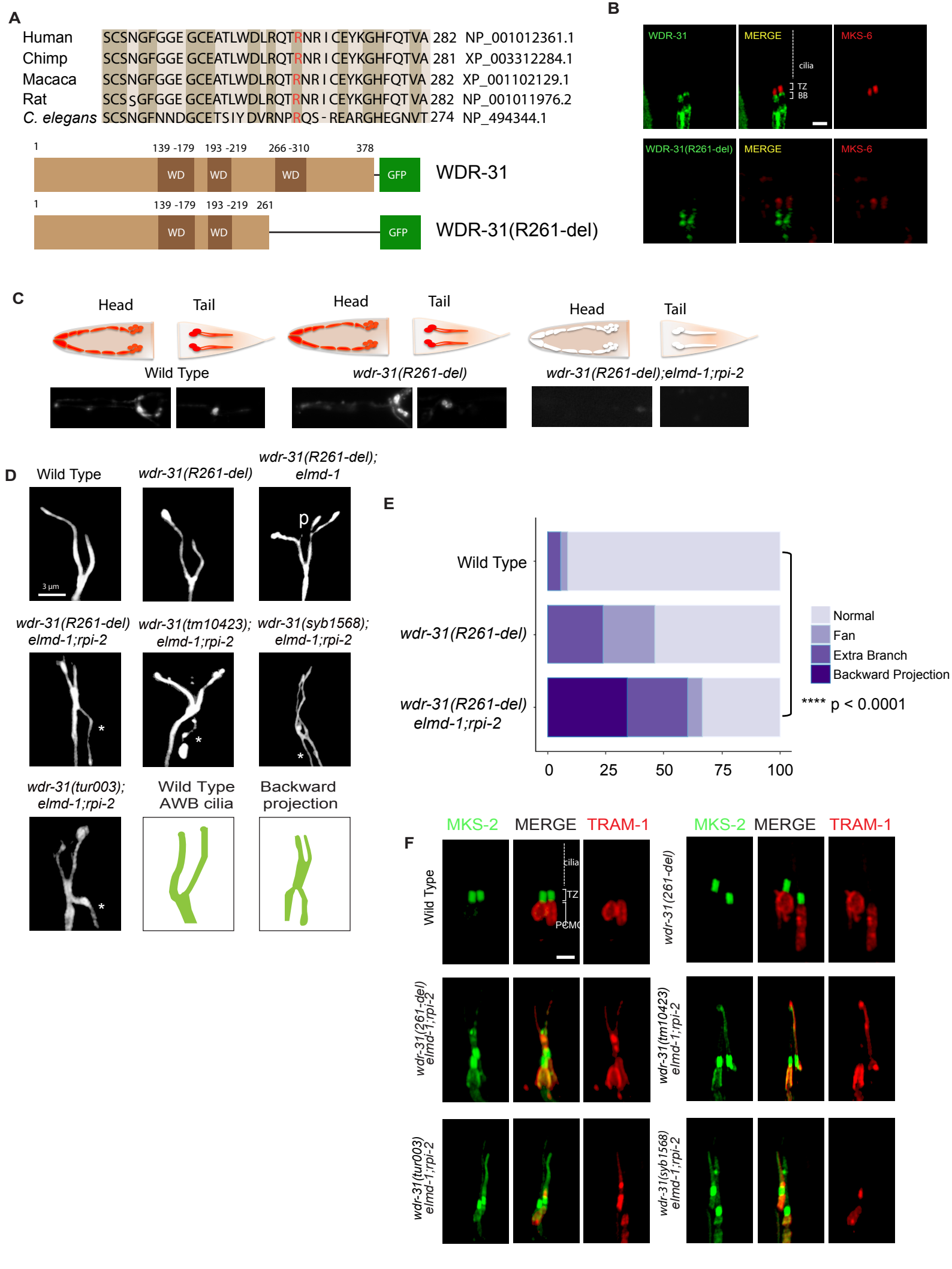
A
Human SCSNGFGGE GCEATLWDLRQTRNR I CEYKGHFQTVA 282 NP_001012361.1
Chimp SCSNGFGGE GCEATLWDLRQTRNR I CEYKGHFQTVA 281 XP_003312284.1
Macaca SCSNGFGGE GCEATLWDLRQTRNR I CEYKGHFQTVA 282 XP_001102129.1
Rat SCS SGFGGE GCEATLWDLRQTRNR I CEYKGHFQT VA 282 NP_001011976.2
C. elegans SCSNGFNNDGCETS I Y DVRNPRQS - REARGHEGNVT 274 NP_494344.1
1
139 -179
193 -219
266 -310
378
WD
WD
WD
GFP
WDR-31
1
139 -179
193 -219
261
WD
WD
GFP
WDR-31(R261-del)
B
WDR-31
MERGE
MKS-6
cilia
TZ
BB
WDR-31(R261-del)
MERGE
MKS-6
C
Head
Tail
Head
Tail
Head
Tail
Wild Type
wdr-31(R261-del)
wdr-31(R261-del);elmd-1;rpi-2
D
Wild Type
wdr-31(R261-del)
wdr-31(R261-del); elmd-1
p
3 µm
wdr-31(R261-del) elmd-1;rpi-2
wdr-31(tm10423); elmd-1;rpi-2
wdr-31(syb1568); elmd-1;rpi-2
wdr-31(tur003); elmd-1;rpi-2
Wild Type AWB cilia
Backward projection
E
Wild Type
wdr-31(R261-del)
wdr-31(R261-del) elmd-1;rpi-2
Normal
Fan
Extra Branch
Backward Projection
**** p < 0.0001
0
25
50
75
100
F
MKS-2
MERGE
TRAM-1
MKS-2
MERGE
TRAM-1
Wild Type
cilia
TZ
PCM
wdr-31(261-del)
wdr-31(261-del) elmd-1;rpi-2
wdr-31(tm10423) elmd-1;rpi-2
wdr-31(tur003) elmd-1;rpi-2
wdr-31(syb1568) elmd-1;rpi-2

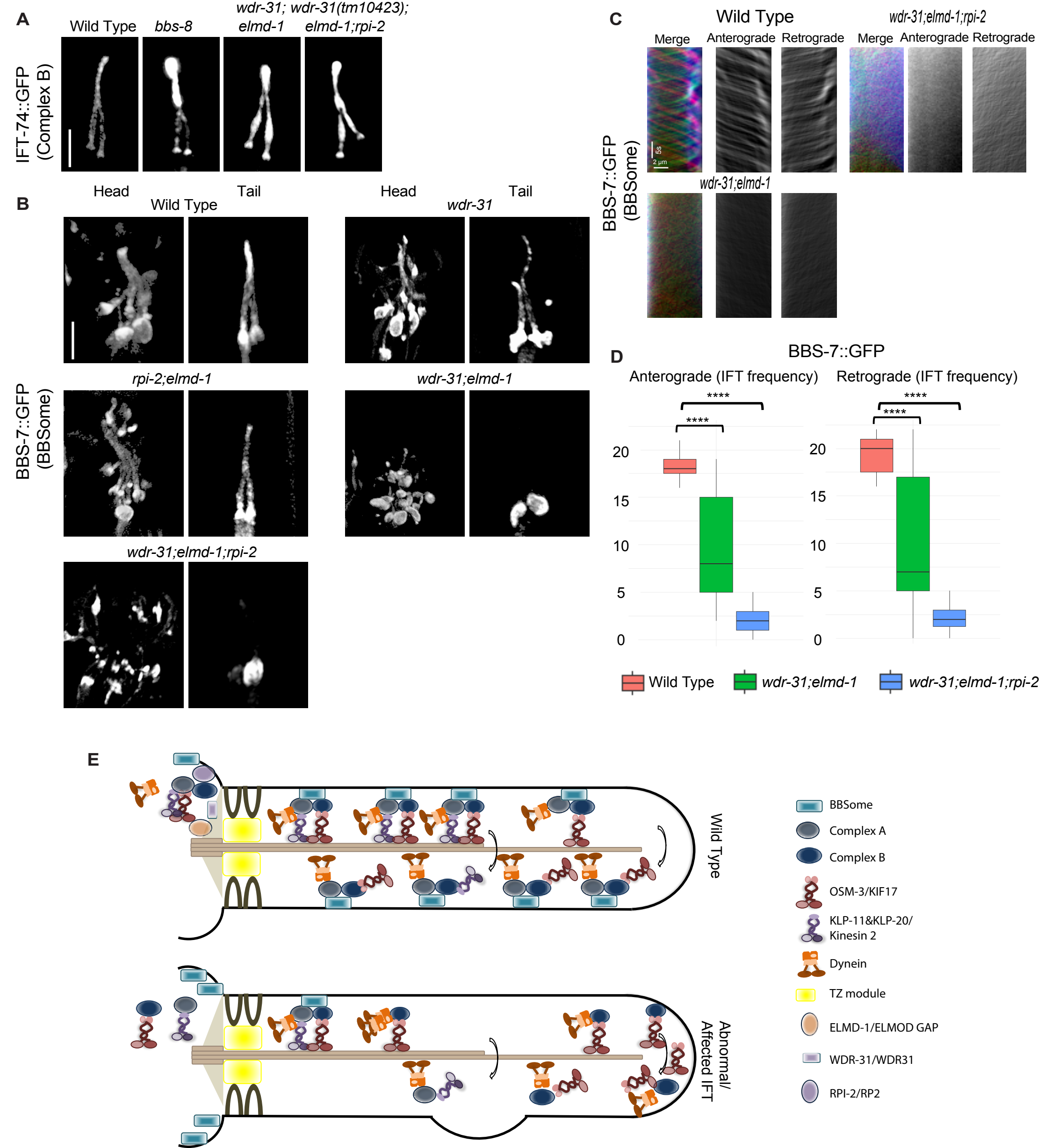
A
Wild Type
bbs-8
wdr-31; wdr-31(tm10423);
elmd-1
elmd-1;rpi-2
IFT-74::GFP
(Complex B)
B
Head
Tail
Wild Type
Head
Tail
wdr-31
BBS-7::GFP
(BBSome)
rpi-2;elmd-1
wdr-31;elmd-1
wdr-31;elmd-1;rpi-2
C
Wild Type
wdr-31;elmd-1;rpi-2
Merge
Anterograde
Retrograde
Merge
Anterograde
Retrograde
BBS-7::GFP
(BBSome)
5s
2 µm
wdr-31;elmd-1
D
BBS-7::GFP
Anterograde (IFT frequency)
Retrograde (IFT frequency)
****
****
****
****
20
15
10
5
0
Wild Type
wdr-31;elmd-1
wdr-31;elmd-1;rpi-2
E
Wild Type
Abnormal/
Affected IFT
BBSome
Complex A
Complex B
OSM-3/KIF17
KLP-11&KLP-20/
Kinesin 2
Dynein
TZ module
ELMD-1/ELMOD GAP
WDR-31/WDR31
RPI-2/RP2